PHYSICAL REVIEW D **95,** 123512 (2017)

Looking through the same lens: Shear calibration for LSST, Euclid, and WFIRST with stage 4 CMB lensing

Emmanuel Schaan,[1,*] Elisabeth Krause,[2] Tim Eifler,[3,4] Olivier Doré,[3,4] Hironao Miyatake,[3,4,5] Jason Rhodes,[3,4] and David N. Spergel[1]

[1]*Department of Astrophysical Sciences, Princeton University, Peyton Hall, Princeton, New Jersey 08544, USA*
[2]*Kavli Institute for Particle Cosmology and Astrophysics, Stanford University, Stanford, California 94305, USA*
[3]*Jet Propulsion Laboratory, California Institute of Technology, Pasadena, California 91109, USA*
[4]*Department of Physics, California Institute of Technology, Pasadena, California 91125, USA*
[5]*Kavli Institute for the Physics and Mathematics of the Universe (Kavli IPMU, WPI), The University of Tokyo, Chiba 277-8582, Japan*

(Received 20 August 2016; published 8 June 2017)

The next-generation weak lensing surveys (i.e., LSST, Euclid, and WFIRST) will require exquisite control over systematic effects. In this paper, we address shear calibration and present the most realistic forecast to date for LSST/Euclid/WFIRST and CMB lensing from a stage 4 CMB experiment ("CMB S4"). We use the COSMOLIKE code to simulate a joint analysis of all the two-point functions of galaxy density, galaxy shear, and CMB lensing convergence. We include the full Gaussian and non-Gaussian covariances and explore the resulting joint likelihood with Monte Carlo Markov chains. We constrain shear calibration biases while simultaneously varying cosmological parameters, galaxy biases, and photometric redshift uncertainties. We find that CMB lensing from CMB S4 enables the calibration of the shear biases down to 0.2%–3% in ten tomographic bins for LSST (below the ∼0.5% requirements in most tomographic bins), down to 0.4%–2.4% in ten bins for Euclid, and 0.6%–3.2% in ten bins for WFIRST. For a given lensing survey, the method works best at high redshift where shear calibration is otherwise most challenging. This self-calibration is robust to Gaussian photometric redshift uncertainties and to a reasonable level of intrinsic alignment. It is also robust to changes in the beam and the effectiveness of the component separation of the CMB experiment, and slowly dependent on its depth, making it possible with third-generation CMB experiments such as AdvACT and SPT-3G, as well as the Simons Observatory.

DOI: 10.1103/PhysRevD.95.123512

I. INTRODUCTION

Understanding the physics of cosmic acceleration is the aim of many ongoing and upcoming imaging surveys such as the Kilo-Degree Survey (KiDS) [1], the Dark Energy Survey (DES) [2,3], the Subaru Hyper Suprime-Cam (HSC) survey [4,5], the Subaru Prime Focus Spectrograph (PFS) [6,7], the Dark Energy Spectroscopic Instrument (DESI) [8], the Large Synoptic Survey Telescope (LSST) [9], the ESA satellite mission Euclid [10], and NASA's Wide-Field Infrared Survey Telescope (WFIRST) [11]. Through gravitational lensing, images of distant sources such as galaxies or the cosmic microwave background (CMB) are distorted by the presence of foreground mass. In the weak regime, lensing produces small distortions, arcminute deflections or ∼1% shear, coherent on degree scales, which are detected statistically. Weak gravitational lensing is sensitive to the growth of structure and the geometry of the universe, making it a powerful probe of dark energy, modifications to general relativity, and the sum of the neutrino masses (see [12] and references therein for a review).

Realizing the full potential of the stage 4 weak lensing surveys (i.e., LSST, Euclid, and WFIRST) requires an exquisite understanding and control of systematics effects [13]. In the case of LSST, the bias and scatter in photometric redshifts need to be controlled to better than a percent [14], which may require more than $\sim 10^5$ galaxy spectra for calibration [15]. Interpreting cosmic shear, i.e., the power spectrum of the weak lensing of galaxies by the large-scale structure in the universe, requires knowledge of the matter power spectrum, down to scales where nonlinear evolution and baryonic effects are important [16–24]. Intrinsic alignments of galaxies, if not mitigated, could contaminate the cosmic shear signal by up to 1%–10% (see [25–28] for a review). Finally, estimating the shear from galaxy shapes may lead to additive and multiplicative biases, typically redshift dependent, which have to be controlled to a high accuracy [14,29]. The shear multiplicative bias is degenerate with the amplitude of the signal, and its time evolution can hide the true evolution of the growth of structure, which probes dark energy and possible modifications to general relativity. Massey *et al.* [29] found

*emmanuel.schaan@gmail.com

that fully exploiting the statistical power of a stage 4 cosmic shear survey requires a shear multiplicative bias of $\lesssim 0.4\%$. The focus of this paper is to show how CMB lensing contributes to reaching this goal.

Many effects contribute to the shear multiplicative bias [29–31], such as inaccuracies in the point-spread function (PSF) or detector effects (e.g., charge transfer inefficiency in CCDs or the brighter-fatter effect). Model biases may occur when estimating galaxy shapes with an inaccurate galaxy profile. Since lensing couples the short and long wavelength modes of a galaxy image, knowing the response of a galaxy image to shear requires knowing the galaxy image to a better resolution than the PSF, leading in practice to a "noisy deconvolution" shape bias. Furthermore, the galaxies used for shear estimation do not form a homogeneous sample, and their detection signal-to-noise ratio (SNR) depends on their shape, leading to a shape selection bias. Correcting this bias perfectly would require knowledge of the galaxy population below the detection threshold [29,30]. State-of-the-art shape algorithms calibrated on simulations (e.g., Refs. [30,31]) reach few-percent accuracy on the shear multiplicative bias. They currently approach the requirements of stage 4 surveys (e.g., Ref. [32]) in the absence of selection bias (i.e., when the galaxy population is known perfectly) and for images with slightly higher signal-to-noise ratios.

Because the shear multiplicative bias is such a critical and difficult systematic for stage 4 weak lensing surveys, alternative methods to calibrate it provide a valuable redundancy. These consistency checks will be crucial in trusting the results, e.g., in the optimistic event where stage 4 weak lensing surveys would find deviations from ΛCDM.

The lensing convergence reconstructed from temperature and polarization of the CMB does not rely on galaxy shape estimation [33–35]. Although CMB lensing is most sensitive to the matter distribution at higher redshifts, the lensing efficiencies for CMB and galaxy lensing overlap, thus potentially allowing us to calibrate the shear multiplicative bias [36–38]. Using a Fisher forecast, Vallinotto [36,37] and Das *et al.* [38] combined all the two-point correlations of galaxy positions, galaxy shapes, and CMB lensing convergence. They showed that adding CMB lensing and galaxy spectroscopic data to a shape catalog allows one to approach the requirements on shear calibration for stage 4 weak lensing surveys. This method is appealing because it is a self-calibration: It relies on the data alone and not on image simulations of the whole galaxy sample. It is a practical example of real synergy between overlapping surveys, where combining probes leads to improved systematics and not just a marginally higher signal-to-noise ratio. CMB lensing has been measured by the WMAP satellite [39,40], the Atacama Cosmology Telescope (ACT) [41–44], the South Pole Telescope (SPT) [45–47], POLARBEAR [48], the Planck satellite [49,50], and the BICEP 2/Keck Array [51]. In the future, Advanced ACT [52], SPT-3G [53], and a stage 4 ground-based CMB experiment (CMB S4) [54,55], as well as the Simons Observatory [56], will provide high fidelity maps of the CMB lensing convergence over a large fraction of the sky.

Recent work applied this method to existing stage 3 data. Liu *et al.* [57] correlated galaxy positions from CFHT with galaxy shapes from CFHT and CMB lensing from Planck. Assuming a fixed cosmology (WMAP or Planck parameters) and known photometric redshift errors, they constrained the shear bias in the CFHT shape catalog, finding a shear bias lower than unity at $2\sigma - 4\sigma$. However, a shift in the cosmological parameters, a different redshift evolution of the galaxy bias, or uncharacterized photometric redshift errors might explain this tension. Similarly, Baxter *et al.* [58] correlated galaxy positions from DES with galaxy shapes from DES and CMB lensing from SPT, to constrain the shear bias and an overall additive photometric redshift bias. The constraints on shear bias are obtained by fixing cosmology and the photo-z bias to fiducial values. Cross-correlations between galaxy shear and CMB lensing have been measured [59–62]. In [63], the combination of galaxy shear and CMB lensing is forecasted to improve dark energy and neutrino mass constraints. In [64], the CMB lensing from Planck and the galaxy lensing from CFHTLenS is measured around CMASS halos, yielding a 15% measurement of a cosmographic distance ratio. Finally, Ref. [65] measured all the two-point correlations of galaxy positions and shear from SDSS and CMB convergence from Planck, and in turn constrained galaxy bias to 2% accuracy, cosmology, shear multiplicative bias to 15% and distance ratio to 10%. While Refs. [57,58,65] currently constrain the shear bias to $\gtrsim 10\%$, far from current state-of-the-art calibrations from simulations, they constitute very encouraging first steps in using CMB lensing and spectroscopic data to calibrate the shear bias.

In this paper, we address the following questions: Can CMB lensing calibrate the shear bias down to the requirements of stage 4 surveys? Is this method competitive with image simulations? Is this possible without arbitrarily fixing cosmological and nuisance parameters? How robust is this calibration to photometric redshift uncertainties and intrinsic alignments? To answer these questions in a realistic way, we simulate the full joint analysis of weak lensing, photometric clustering, and CMB lensing. We compute the full covariances for all the two-point auto-correlations and cross-correlations, including the non-Gaussian covariances which dominate on small scales. We analyze the full likelihood function with Monte Carlo Markov chains (MCMC), allowing for a potentially non-Gaussian posterior distribution. This is particularly relevant when assessing nonlinear degeneracies between parameters. We compare these MCMC forecasts with Fisher forecasts, thus assessing potential departures from Gaussianity of the posterior distributions. We test the robustness of the method by simultaneously varying

shear biases, cosmological parameters, galaxy biases and photometric redshift uncertainties (bias in each tomographic bin and overall scatter), and by contaminating the simulated data with intrinsic alignment. We extend the COSMOLIKE [66] framework to include CMB lensing and produce the most realistic forecast to date for LSST/Euclid/WFIRST and CMB lensing from a stage 4 CMB experiment. Given the importance of this result, and as an input for the design of CMB S4, we vary the depth, resolution, and maximum multipole of the CMB experiment and show the robustness of this shear calibration method.

This paper is organized as follows. In Sec. II we describe the observables considered, the survey specifications, the systematic effects included, and the simulated likelihood. In Sec. III A we revisit the LSST requirements and show that self-calibration of the shear biases with LSST alone is possible down to 1%–2%. The calibration of shear multiplicative bias down to the LSST requirements by using stage 4 CMB lensing is presented in Sec. III B, along with the impact of intrinsic alignments. We show the importance of sensitivity and resolution for CMB S4 in Sec. IV A, the robustness to photometric redshift uncertainties in Sec. IV B and to nonlinearities and baryonic effects in Sec. IV C, and present forecasts for Euclid and WFIRST instead of LSST in Sec. IV E.

II. SIMULATED JOINT ANALYSIS OF LSST AND CMB S4: METHOD

A. Observables: g, $\kappa_{\rm gal}$, $\kappa_{\rm CMB}$

We use the projected galaxy density field g, the convergence $\kappa_{\rm gal}$ from galaxy shapes, and $\kappa_{\rm CMB}$ from CMB lensing reconstruction as probes of the matter density field. We consider two distinct galaxy samples for g and $\kappa_{\rm gal}$, with distinct redshift distributions and tomographic bins, as detailed in Sec. II C. Each observable $A \in \{g, \kappa_{\rm gal}, \kappa_{\rm CMB}\}$ is a projection of the density contrast δ, weighted by an efficiency kernel W_A:

$$A(\hat{n}) = \int d\chi W_A(\chi)\delta(\chi\hat{n},\chi). \quad (1)$$

Thus, the cross-spectrum C_ℓ^{AB} of observables A, B is related to the matter power spectrum P_m via

$$C_\ell^{AB} = \int \frac{d\chi}{\chi^2} W_A(\chi) W_B(\chi) P_m\left(k = \frac{\ell + 1/2}{\chi}, \chi\right), \quad (2)$$

in the Limber and flat sky approximations. Throughout, we assume a flat cosmology and therefore equate comoving radial and transverse distances. For the projected density field g_i in redshift bin i, the efficiency kernel is

$$W_{g_i}(\chi) = b_g(z)\frac{1}{n_i}\frac{dn_i}{dz}\frac{dz}{d\chi}, \quad \text{with} \quad n_i = \int dz \frac{dn_i}{dz}, \quad (3)$$

and dn_i/dz is the redshift distribution of the galaxies in the ith bin. For a source at comoving distance χ_S, the lensing efficiency is

$$W_\kappa(\chi,\chi_S) = \frac{3}{2}\left(\frac{H_0}{c}\right)^2 \Omega_m^0 \frac{\chi}{a(\chi)}(1-\chi/\chi_S). \quad (4)$$

Thus, the CMB lensing efficiency is simply $W_{\kappa_{\rm CMB}}(\chi) = W_\kappa(\chi,\chi_{\rm LSS})$, where $\chi_{\rm LSS}$ is the comoving distance to the surface of last scattering at $z \sim 1100$ (see curve in Fig. 2). For the convergence $\kappa_{{\rm gal},i}$ in the tomographic bin i, the efficiency kernel is obtained by integrating over the source distribution in the same bin:

$$W_{\kappa_{{\rm gal},i}}(\chi) = \frac{1}{n_{{\rm source},i}} \int dz_S \frac{dn_{{\rm source},i}}{dz_S} W_\kappa(\chi,\chi(z_S)). \quad (5)$$

In this simulated analysis, we compute all the cross-spectra and autospectra of g, $\kappa_{\rm gal}$, and $\kappa_{\rm CMB}$ in different tomographic redshift bins. The analysis therefore includes galaxy clustering ($C_\ell^{g_i g_j}$), galaxy-galaxy lensing ($C_\ell^{g_i \kappa_{{\rm gal},j}}$), galaxy-CMB lensing ($C_\ell^{g_i \kappa_{\rm CMB}}$), cosmic shear tomography ($C_\ell^{\kappa_{{\rm gal},i}\kappa_{{\rm gal},j}}$), CMB lensing power spectrum ($C_\ell^{\kappa_{\rm CMB}\kappa_{\rm CMB}}$), and CMB lensing-galaxy lensing ($C_\ell^{\kappa_{\rm CMB}\kappa_{{\rm gal},j}}$). Our specific assumptions about CMB S4 and LSST are detailed in the next sections, as is the treatment of the systematic effects.

B. CMB S4 specifications

We simulate a stage 4 CMB experiment [54,55], with specifications presented in Fig. 1. We assume full overlap with LSST, high resolution (beam FWHM $= 1'$), and sensitivity (white noise level 1 $\mu K'$).

Following [54], we assume that the resulting cleaned CMB temperature map covers multipoles from $\ell_{\rm min} = 30$ to $\ell_{\rm max} = 3000$, and that the resulting E and B polarization maps extend from $\ell_{\rm min} = 30$ to $\ell_{\rm max} = 5000$. In this paper, we use the reconstructed convergence map $\kappa_{\rm CMB}$ between $\ell = 30$ and $\ell = 5000$. The value of $\ell_{\rm max}$ is mainly a statement about component separation, thought to be more effective in polarization than temperature. Accessing the low multipoles down to $\ell_{\rm min} = 30$ in temperature and polarization is very challenging from the ground and will likely require including Planck data. However, these low temperature and polarization multipoles are not essential to the lens reconstruction, which relies mostly on the smaller scales: Reconstructing the $\ell_{\rm min} = 30$ modes of the CMB lensing convergence does not require the $\ell_{\rm min} = 30$ modes of temperature or polarization. As an input for the design of CMB S4, we quantify the separate impacts of resolution, depth, and effectiveness of component separation in Sec. IV A.

Our likelihood analysis uses the reconstructed convergence $\kappa_{\rm CMB}$ from CMB S4 and assumes the minimum

CMB S4 specifications	
Ω_s	18,000 deg^2 ($f_{sky} = 44\%$)
beam	FWHM$= 1'$
white noise	$1\mu K'$ for T; $1.4\mu K'$ for E,B
ℓ_{min}	30 for T, E, B, κ_{CMB}
ℓ_{max}	3000 for T; 5000 for E, B, κ_{CMB}

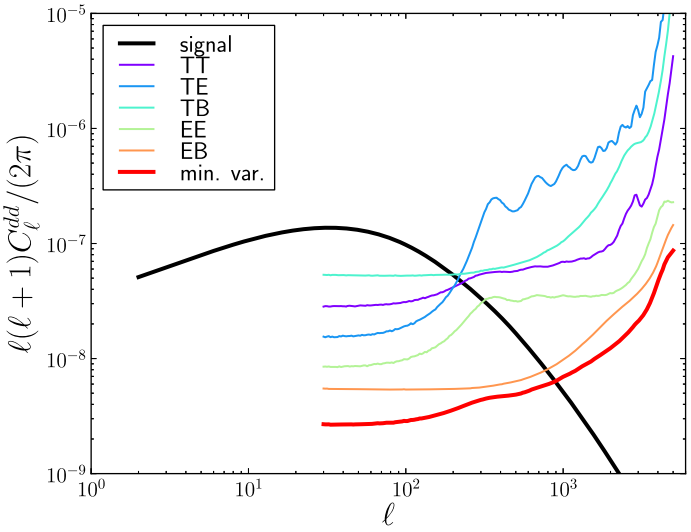

FIG. 1. Assumed specifications for CMB S4. Left panel: Assumed survey area, resolution, sensitivity, and ℓ limits. The cutoff ℓ_{max} is determined by our ability to effectively remove foregrounds with multifrequency data, and the values assumed here represent reasonable assumptions. Right panel: Corresponding noise per ℓ mode for the various quadratic estimators (colored lines) and for the minimum-variance quadratic estimator (solid black line), compared to the amplitude of the CMB lensing signal (dashed black line). The CMB lensing convergence is cosmic variance limited up to $\ell = 1000$.

variance quadratic estimator from Refs. [33,34]. This minimum variance estimator is the optimal linear combination of the quadratic estimators from temperature and E and B polarizations. The corresponding reconstruction noise is shown in Fig. 1: The reconstructed convergence is cosmic variance limited up to $\ell = 1000$. At the resolution and sensitivity considered, iterative techniques making use of the full likelihood function for the CMB convergence may improve the reconstruction noise by a factor of order unity, compared to the minimum variance quadratic estimator [67,68]. Using only the quadratic estimators gives a conservative forecast for CMB S4 lensing.

We do not include temperature and polarization power spectra from CMB S4, nor Planck priors on cosmological parameters: We wish to use the minimal number of probes in the shear calibration. Furthermore, given the high statistical signal-to-noise ratio, a consistent analysis might need to account for correlations between the CMB temperature and polarization and the large-scale structure. We found that including Planck priors on cosmological parameters improves the shear calibration by several tens of percent.

LSST specifications	
Ω_s	18,000 deg^2
source distribution	$dn_{source}/dz \propto z^\alpha e^{-(z/z_0)^\beta}$, $\alpha = 1.27, \beta = 1.02, z_0 = 0.5$, $n_{source} = 26$ arcmin^{-2}, 10 bins, $\sigma_\epsilon = 0.26$
lens distribution	$dn_{lens}/dz \propto \chi(z)^2/H(z)$, $n_{lens} = 0.25$ arcmin^{-2}, 4 bins

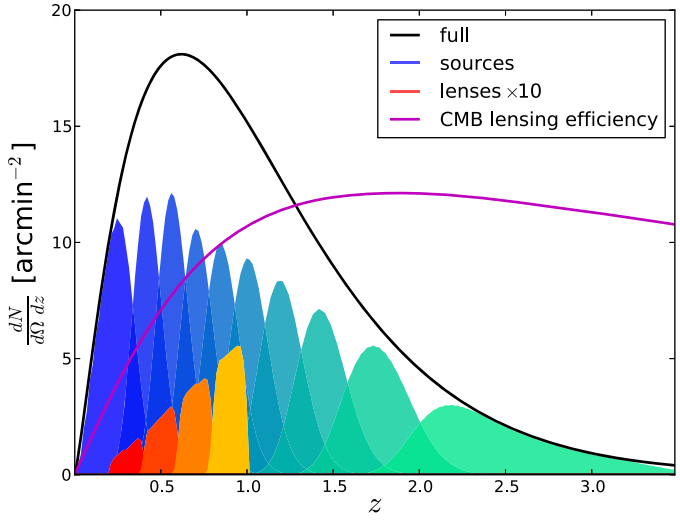

FIG. 2. Assumed specifications for LSST [9], following [69]. The left panel shows the survey area, galaxy density, redshift distribution of the sources, and shape noise. The right panel shows the full redshift distribution of the source galaxies (black curve), split into ten tomographic bins (blue filled curves). The lens sample is redMaGiC-like [70], split into four lens bins (red-yellow filled curves, multiplied by 10 to be visible on the same scale). Overlaid is the CMB lensing efficiency kernel (magenta line).

C. LSST specifications

Closely following [69], we simulate a LSST-like survey [9] over a total area $\Omega_s = 18,000$ deg^2. The assumed specifications are presented in Fig. 2.

We assume the source redshift distribution to follow $dn_{\rm source}/dz \propto z^\alpha e^{-(z/z_0)^\beta}$, with $\alpha = 1.27, \beta = 1.02, z_0 = 0.5$, with a total number density $n_{\rm source} = 26$ arcmin^{-2} [71], and a shape noise $\sigma_\epsilon = 0.26$ in each ellipticity component. We split the source galaxies into ten tomographic redshift bins.

The assumed galaxy lens sample is similar to the redMaGiC sample [70], with a constant comoving volume density $\bar{n}_{\rm lens}(z) = 10^{-3}(h/{\rm Mpc})^3$ and corresponding redshift distribution $dn_{\rm lens}/dz \propto \chi(z)^2/H(z)$, giving a total number density of $n_{\rm lens} = 0.25$ arcmin^{-2}. We split these galaxies into four tomographic bins. The lens sample is also used as the clustering sample: The same projected galaxy density field g is used for clustering and lensing-tracer correlations. In both cases, we only use the ℓ modes with $\ell \geq 20$ and $2\pi\chi(z_{\rm mean})/\ell > 10$ Mpc/h, corresponding to the smallest scale where we assume linear biasing to be valid. In practice, this corresponds to $\ell_{\rm max} = 420, 714, 930$, and 1212, respectively, for the four redshift bins. We introduce the effective galaxy bias $b_{\rm g}^i$ for each bin i, as four nuisance parameters. Several comments are in order. We have selected a clustering and lens sample with excellent photo-z accuracy (see next subsection), in order to get a robust shear calibration. For this reason, we have restricted the lens sample to $z < 1$, beyond which photo-z accuracy is expected to degrade considerably. This limits the signal-to-noise ratio in clustering and tracer-lensing correlations considerably. As a result, our forecast for shear calibration from data combinations involving clustering and tracer lensing should be considered very conservative. We note however that the comoving volume density of this redMaGiG-like sample is not limiting: The galaxy shot noise in this sample is subdominant on almost all the scales we retain.

For the convergence field $\kappa_{\rm gal}$, we use all the modes $20 \leq \ell \leq 5000$. This is the current baseline for lensing forecasts with LSST. On the smallest scales, baryonic effects in the matter power spectrum may constitute a source of systematic error. We discuss it in the next subsection.

D. Systematics and nuisance parameters

In addition to the basic LSST survey parameters summarized above, this section specifies our detailed assumptions on systematic uncertainties affecting the LSST galaxy samples.

1. Photometric redshift uncertainties

We assume Gaussian photometric redshift uncertainties, with a bias Δ_z and scatter σ_z, such that

$$p(z_{\rm ph}|z) = \frac{1}{\sqrt{2\pi\sigma_z^2}} \exp\left[-\frac{(z_{\rm ph} - z - \Delta_z)^2}{2\sigma_z^2}\right] \quad (6)$$

is the probability of measuring the photo-z $z_{\rm ph}$ given a galaxy with true redshift z. This approach neglects catastrophic photo-z failures [72]. Realistic distributions for $p(z_{\rm ph}|z)$ can be much more complex; however, a careful treatment of photo-z outliers is beyond the scope of this paper. We split the lens sample into four tomographic bins $z \in (0.2-0.4), (0.4-0.6), (0.6-0.8), (0.8-1)$. We split the source sample into ten tomographic bins with equal numbers of objects per bin. These bins are defined by sharp photo-z cuts and therefore have overlapping true redshift distributions [73]:

$$\frac{dn_{{\rm lens/source},i}}{dz} = \frac{dn_{\rm lens/source}}{dz} \int_{z_{\rm ph} \in {\rm bin}\, i} dz_{\rm ph} p(z_{\rm ph}|z). \quad (7)$$

These redshift distributions are shown in Fig. 2. The large number of tomographic bins for the lens and source samples is justified *a posteriori* by the good SNR and low correlation coefficient for the various ℓ bins and tomographic bins. For each lens or source bin, we introduce a bias $\Delta_{z,{\rm lens/source},i}$, as well as an overall scatter $\sigma_{z,{\rm lens/source}}/(1+z)$, resulting in 16 nuisance parameters. We marginalize over these nuisance parameters with priors as indicated in Table I.

2. Multiplicative shear bias

We describe shear calibration uncertainties via an overall shear multiplicative bias m_i for each source bin i, resulting in ten nuisance parameters: $\kappa_{{\rm gal},i} \to (1+m_i)\kappa_{{\rm gal},i}$. The goal of this analysis is to forecast the constraints on m_i, with and without priors. This parametrization of the multiplicative shear bias follows [75] and is the one used in state-of-the-art galaxy lensing data analysis (e.g., Refs. [30,31]). Several comments are in order.

For a given redshift bin, we assume that the shear bias is a scalar quantity. In principle, the observed shear is a tensor, so the multiplicative bias on each component of the tensor could be different. In practice though, the two components of the multiplicative bias are found to be similar when estimated separately [30]. This justifies our assumption of a scalar shear multiplicative bias.

We assume that the shear biases m_i for the various source bins are independent. This is likely not the case, for at least two reasons. First, whatever process causes the shear bias (e.g., errors in the modeling of the galaxy population or morphologies) is likely to vary smoothly with redshift. Second, uncertainties in the photometric redshifts of galaxies cause a mixing between the galaxies of neighboring bins, which tends to equalize the shear bias in the corresponding bins. As a result, one would expect some correlation between the shear biases of the different redshift

TABLE I. We vary 37 parameters in the simulated likelihood analysis, including 7 cosmological parameters, 4 galaxy biases, 16 photo-z parameters, and 10 shear biases. For each parameter, the fiducial value is shown, as well as the prior [either flat (min, max) or Gaussian (μ, σ)]. Priors for the nuisance parameters follow [69]. The fiducial values for the cosmological parameters follow [74].

Parameter	Fiducial	Prior
	Cosmology	
$\Omega_{\rm m}^0$	0.3156	flat (0.1, 0.6)
σ_8	0.831	flat (0.6, 0.95)
$n_{\rm s}$	0.9645	flat (0.85, 1.06)
w_0	-1	flat $(-2, 0)$
$w_{\rm a}$	0	flat $(-2.5, 2.5)$
$\Omega_{\rm b}^0$	0.0492	flat (0.04, 0.055)
h_0	0.6727	flat (0.6, 0.76)
	Galaxy bias	
$b_{\rm g}^1$	1.35	flat (0.8, 2.0)
$b_{\rm g}^2$	1.5	flat (0.8, 2.0)
$b_{\rm g}^3$	1.65	flat (0.8, 2.0)
$b_{\rm g}^4$	1.8	flat (0.8, 2.0)
	Photo-z: Lens sample	
$\Delta_{z,{\rm lens},i}$	0	Gauss (0, 0.0004)
$\sigma_{z,{\rm lens}}/(1+z)$	0.01	Gauss (0.01, 0.0006)
	Photo-z: Source sample	
$\Delta_{z,{\rm source},i}$	0	Gauss (0, 0.002)
$\sigma_{z,{\rm source}}/(1+z)$	0.05	Gauss (0.05, 0.003)
	Shear calibration	
m_i	0	Gauss (0, 0.004) or none

bins. One could therefore include priors on the shear biases of the various redshift bins to take into account this correlation. However, deriving such realistic priors is beyond the scope of this paper. Furthermore, making the shear biases correlated effectively reduces the number of these nuisance parameters, which should therefore improve the resulting constraints. In conclusion, our assumption of independent multiplicative biases is conservative, and adding extra knowledge on their correlations will only improve the results presented here.

We ignore any scale dependence (i.e., ℓ dependence) of the shear biases. Scale dependence of the shear biases can be marginalized over if a template exists, i.e., if the scale dependence has a known shape [76]. This is not currently done in state-of-the-art galaxy lensing analyses (e.g., Refs. [30,31]), and proposing realistic templates for the scale dependence of the shear bias is beyond the scope of this paper.

3. Intrinsic alignments

To assess the potential contamination from galaxy intrinsic alignments (IA), we include the IA contamination in the data vector but do not account for the contamination in the analysis. We model IA using the nonlinear linear alignment (NLA) model [77–79] for red galaxies, and neglect the plausible, but much weaker alignment of blue galaxies [80–82]. We calculate the expected intrinsic alignment amplitude by averaging the observed redshift and luminosity dependence of the intrinsic alignment amplitude of red galaxies in the MegaZ-LRG sample [83] over the luminosity function of source galaxies, for which we extrapolate the r-band luminosity function measurements from the GAMA survey [84] to LSST depth (see [85] for details).

Unaccounted IA biases the shear estimated from galaxy shapes and can therefore affect all cross-correlations involving at least one $\kappa_{\rm gal}$. We calculate the contamination of $g\kappa_{\rm gal}$ and $\kappa_{\rm gal}\kappa_{\rm gal}$ following [86], and the contamination of $\kappa_{\rm gal}\kappa_{\rm CMB}$ following [87,88].

A detailed study of all existing IA models and mitigation techniques is beyond the scope of this paper; in the case of cosmic shear with LSST, we refer the reader to [85].

4. Nonlinearities and baryonic effects

We account for nonlinearities in the covariance matrix by including the nonlinear trispectrum terms as well as the supersample covariances [89–93] as in [69].

For the projected density field g, we discard the small scales (see previous subsection) where linear bias might no longer be valid. This limits the potential effect of baryons. For the lensing convergence $\kappa_{\rm gal}$, we do not include any uncertainty in the modeling of the nonlinear power spectrum or the baryonic effects. However, we show in Sec. IV C that the shear calibration is only degraded by 10%–40% when varying the maximum multipole $\ell_{\rm max}$ from our fiducial value of 5000 down to 1000.

5. Biases in the CMB lensing reconstruction

The quadratic estimators for CMB lensing exploit the statistical isotropy of the primary CMB. Any component that breaks this statistical isotropy will therefore contribute to the reconstructed $\kappa_{\rm CMB}$ map. This the case of the cosmic infrared background, as well as radio point sources and thermal Sunyaev-Zel'dovich clusters, whether they are resolved or not. These sources may contaminate the convergence map and its power spectrum at the subpercent to percent level, but mitigation techniques exist [94,95]. In this analysis, we do not take into account these potential biases.

E. Likelihood analysis

Our simulated data vector for the joint LSST and CMB S4 analysis consists of all the autospectra and cross-spectra of galaxy projected density, galaxy convergence, and CMB convergence for all the lens and source bins:

$$\mathbf{D}_{\mathrm{LSST\&CMB\,S4}} = \Big(\underbrace{C_\ell^{g_i g_j}}_{\text{clustering}}, \underbrace{C_\ell^{g_i \kappa_{\mathrm{CMB}}}}_{\text{galaxy-CMB lensing}}, \underbrace{C_\ell^{g_i \kappa_{\mathrm{gal},j}}}_{\text{galaxy-galaxy lensing}}, \underbrace{C_\ell^{\kappa_{\mathrm{CMB}} \kappa_{\mathrm{CMB}}}}_{\text{CMB lensing auto}}, \underbrace{C_\ell^{\kappa_{\mathrm{CMB}} \kappa_{\mathrm{gal},j}}}_{\text{CMB lensing-galaxy lensing}}, \underbrace{C_\ell^{\kappa_{\mathrm{gal},i} \kappa_{\mathrm{gal},j}}}_{\text{shear tomography}} \Big). \quad (8)$$

Again, we note that our LSST and CMB S4 analysis does not include temperature and polarization power spectra from CMB S4, only the convergence κ_{CMB}. For comparison purposes, we also consider a LSST-only analysis:

$$\mathbf{D}_{\mathrm{LSST}} = \Big(\underbrace{C_\ell^{g_i g_j}}_{\text{clustering}}, \underbrace{C_\ell^{g_i \kappa_{\mathrm{gal},j}}}_{\text{galaxy-galaxy lensing}}, \underbrace{C_\ell^{\kappa_{\mathrm{gal},i} \kappa_{\mathrm{gal},j}}}_{\text{shear tomography}} \Big). \quad (9)$$

Finally, for the purpose of calibrating the shear bias, it is useful to compare the following two combinations:

$$\mathbf{D}_{\mathrm{Combi\,1}} = \Big(\underbrace{C_\ell^{\kappa_{\mathrm{CMB}} \kappa_{\mathrm{CMB}}}}_{\text{CMB lensing auto}}, \underbrace{C_\ell^{\kappa_{\mathrm{CMB}} \kappa_{\mathrm{gal},j}}}_{\text{CMB lensing-galaxy lensing}}, \underbrace{C_\ell^{\kappa_{\mathrm{gal},i} \kappa_{\mathrm{gal},j}}}_{\text{shear tomography}} \Big)$$

$$\mathbf{D}_{\mathrm{Combi\,2}} = \Big(\underbrace{C_\ell^{g_i g_j}}_{\text{clustering}}, \underbrace{C_\ell^{g_i \kappa_{\mathrm{CMB}}}}_{\text{galaxy-CMB lensing}}, \underbrace{C_\ell^{g_i \kappa_{\mathrm{gal},j}}}_{\text{galaxy-galaxy lensing}} \Big). \quad (10)$$

Combination 1 corresponds to the joint analysis of CMB lensing and LSST galaxy shapes through their autocorrelations and cross-correlations. It uses only lensing-lensing correlations. This combination is natural since the CMB is distorted by the same foreground mass distribution as the galaxy shapes (although with a slightly different efficiency kernel), so one could compare the two convergence maps directly, which can be done with the autospectra and cross-spectra of κ_{CMB} and κ_{gal}.

Combination 2 compares CMB lensing and galaxy shapes through cross-correlation with the lens sample, and it adds clustering. It uses tracer-lensing and tracer-tracer correlations. This combination has the advantage of only using cross-correlations of the convergence fields, which are less prone to systematic effects than autocorrelations. As we will show, this combination has slightly lower statistical SNR but is less affected by intrinsic alignment contamination (see Sec. III B). It is also less sensitive to uncertainties in the small-scale power spectrum: Because of our ℓ cuts in the tracer population, the signal is not affected by comoving scales below 10 Mpc/h. This is not the case for lensing-lensing correlations, for which a fixed angular scale receives contributions from arbitrarily small comoving scales.

The various data vectors are computed assuming the survey parameters in Figs. 1 and 2, and the fiducial parameters in Table I. We wish to constrain the parameters in Table I from the mock data vector $\mathbf{D}$. To give visual intuition on the effect of cosmological and nuisance parameters on the observables in $\mathbf{D}$, we show the logarithmic derivatives of $\mathbf{D}$ in Appendix A. These give insight into the degeneracies between cosmological and nuisance parameters. We assume a Gaussian likelihood for the data and ignore the dependence of the covariance matrix on parameters (see [96–98] for the impact of varying the covariance matrix and practical implementations):

$$\ln \mathcal{L}_{(\mathbf{D}|\Theta)} = -\frac{1}{2} (\mathbf{D} - \mathbf{M}_{(\Theta)})^t C^{-1} (\mathbf{D} - \mathbf{M}_{(\Theta)}) + \text{constant}, \quad (11)$$

where $\mathbf{M}_{(\Theta)}$ is the model for the data $\mathbf{D}$, computed in the same way as the data vector but evaluated at the parameters Θ instead of their fiducial value. The Gaussian approximation is most accurate at high ℓ, where the C_ℓ estimator averages over a large number of modes and the central limit theorem applies. As shown in [99], varying the covariance matrix in the Gaussian likelihood may overestimate the information in the data, by including spurious information from the variance of the data vector. Keeping the covariance matrix fixed is therefore a conservative choice, as this includes only the information from the mean data vector.

We explore the posterior distribution with MCMC sampling, using the code EMCEE [100]. This method is appropriate for potentially non-Gaussian posterior distributions. This is relevant in the case of nonlinear degeneracies. We show the convergence of the MCMC chains in Appendix B. We also perform Fisher forecasts and validate them against the MCMC forecasts in Appendix B. Confidence intervals from MCMC and Fisher agree to better than 5%, which is the result of both the convergence of the MCMC chains and the near-Gaussianity of the posterior for the shear biases. As explained earlier, we do not include Planck priors on cosmological parameters.

The covariance matrix is shown in Fig. 3 and includes the Gaussian and non-Gaussian contributions (including

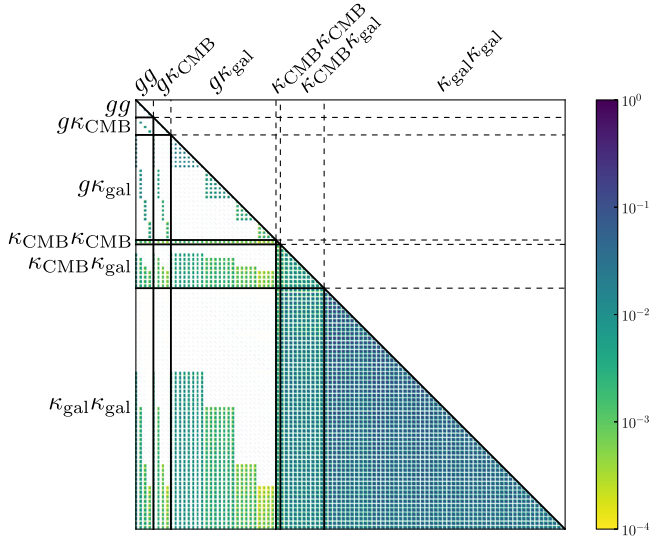

FIG. 3. Correlation coefficient matrix for the full set of observables $\mathbf{D}_{\rm LSST\&CMB\,S4}$ (i.e., clustering, galaxy-CMB lensing, galaxy-galaxy lensing, CMB lensing auto, CMB lensing-galaxy lensing, shear tomography). The matrix is 2450×2450 and includes galaxy clustering, galaxy-galaxy lensing, and shear tomography, as well as CMB lensing, galaxy-CMB lensing, and galaxy lensing-CMB lensing. The details of the calculation are presented in Appendix A of [69]. The reader can zoom in to identify individual matrix elements.

the supersample covariance [69,89–93]). These covariances are computed analytically with COSMOLIKE [66], using Halofit for the nonlinear power spectrum and a halo model for the trispectrum, as in [69] (see their Appendix A). The most notable additional component here is the noise from CMB lensing reconstruction, described in Sec. II B.

From the data vector and the covariance matrix, we compute the individual and combined SNR for the various probes. These are shown in Table II. Note that the statistical SNR is only a good figure of merit when predicting the constraint on a single parameter, the amplitude of the signal, in the absence of nuisance parameters. Instead, we present it here in order to give intuition about the relative statistical weight of each probe. From Table II, we see that each probe will be measured with high significance, with SNR $\sim$ 100–1000.

The SNR in cosmic shear is higher than in galaxy-galaxy lensing and clustering, which is due to our very conservative choice of tracer sample. As explained earlier, in order to get a robust shear calibration and a conservative forecast, we restrict our tracer to $z < 1$ where photo-z uncertainties are very well understood. We also discard the small scales, where linear bias breaks down and a more realistic halo occupation distribution model would be required. Again, this choice severely limits the signal-to-noise ratio in clustering and tracer-lensing correlations.

The total SNR for LSST and CMB S4 lensing is only $\sim$16% higher than that of LSST alone. However, this does not mean that adding CMB S4 lensing is pointless. Indeed, our goal is not to reduce the statistical error bars compared to LSST alone, but instead to constrain systematics by breaking degeneracies, due to the fact that CMB lensing is not affected by the same systematics as galaxy lensing. The SNR does not take into account nuisance parameters and their priors. As we show later, CMB lensing from S4 basically replaces a prior on the shear biases. We discuss this in more detail in the next section.

We also note that CMB lensing and galaxy lensing are relatively well matched in terms of SNR: The SNR in CMB

TABLE II. Individual and combined SNRs, giving insight on the statistical weight of each probe included in the joint analysis. These include Gaussian and non-Gaussian cosmic variance. All probes will be measured at high significance with LSST and CMB S4. The SNR in cosmic shear is higher than in galaxy-galaxy lensing and clustering, which is due to our very conservative choice of tracer sample. CMB lensing from CMB S4 adds a small contribution to the total statistical significance, but it will be important in breaking degeneracies and calibrating the shear multiplicative bias. The SNR gives us an idea of the relative statistical weight of the various observables. However, it does not take into account the presence of nuisance parameters and their priors. As we show later, CMB lensing from S4 basically replaces a prior on the shear multiplicative biases.

LSST and CMB S4	SNR
Individual probes	
Clustering (gg)	377
Galaxy-galaxy lensing: $g\kappa_{\rm gal}$	276
Galaxy-CMB lensing: $g\kappa_{\rm CMB}$	154 (56% of $g\kappa_{\rm gal}$)
Shear tomography: $\kappa_{\rm gal}\kappa_{\rm gal}$	532
CMB lensing auto: $\kappa_{\rm CMB}\kappa_{\rm CMB}$	401 (75% of $\kappa_{\rm gal}\kappa_{\rm gal}$)
Galaxy lensing-CMB lensing: $\kappa_{\rm gal}\kappa_{\rm CMB}$	370
Combinations	
LSST: $gg, g\kappa_{\rm gal}, \kappa_{\rm gal}\kappa_{\rm gal}$	620
Combination 1: $\kappa_{\rm CMB}\kappa_{\rm CMB}, \kappa_{\rm CMB}\kappa_{\rm gal}, \kappa_{\rm gal}\kappa_{\rm gal}$	647
Combination 2: $gg, g\kappa_{\rm CMB}, g\kappa_{\rm gal}$	403
Full: $gg, g\kappa_{\rm CMB}, g\kappa_{\rm gal}, \kappa_{\rm CMB}\kappa_{\rm CMB}, \kappa_{\rm CMB}\kappa_{\rm gal}, \kappa_{\rm gal}\kappa_{\rm gal}$	718 (16% more than LSST alone)

lensing autocorrelation is 75% of the SNR in cosmic shear. This justifies combining the two and drives the calibration of the shear multiplicative biases.

III. SHEAR CALIBRATION FOR LSST: REQUIREMENTS AND SELF-CALIBRATION WITH AND WITHOUT CMB S4 LENSING

A. LSST requirements and self-calibration

In this subsection, we revisit the shear multiplicative bias requirements for LSST [29,101]. We assess the degradation in cosmological parameters as a function of the prior on the shear biases m_i, while jointly fitting for cosmological parameters, galaxy biases, and photo-z uncertainties.

Figure 4 shows the degradation in cosmological parameters as a function of the prior on m_i. The left panel shows the case of cosmic shear alone, while the right panel shows the LSST combination (cosmic shear, galaxy-galaxy lensing, clustering). In both cases, we vary cosmological parameters as well as all the nuisance parameters in Table I. For cosmic shear alone (left panel), we find that a prior on m_i of 0.005 produces a 10% degradation in cosmological parameters compared to a perfect shear calibration. This degradation is somewhat smaller than the 30%–70% found in [14] (in their Fig. 4), likely due to our marginalization of photo-z uncertainties. Furthermore, Refs. [14,29] quote requirements for LSST shear calibration similar to our value of 0.5%, and we will therefore retain this value in the rest of the paper. The left panel of Fig. 5 also shows that self-calibration of the shear is possible from cosmic shear alone. This can be understood intuitively as follows. The dependence of cosmic shear in the m_i is purely multiplicative on all scales, whereas the dependence in other cosmological and nuisance parameters changes with scale: For instance, the cosmic shear power spectrum scales as σ_8^2 in the linear regime and as σ_8^3 in the nonlinear regime (see Fig. 14 in Appendix A). By including both large and small scales, the degeneracy with the shear bias can be broken. We find a degradation of up to 50% in cosmological parameters when completely relaxing the priors on shear calibration. This is again more optimistic compared to [14], who found a factor of 2 degradation, and is again likely due to our marginalization of photo-z uncertainties.

We reproduce this analysis in the case of the full LSST (cosmic shear, galaxy-galaxy lensing, clustering), shown in the right panel of Fig. 4. Since clustering and galaxy-galaxy lensing have different dependences on the shear biases (if any), adding them allows for a better self-calibration of the shear and a reduction in the degradation in cosmological parameters. Indeed, a 0.5% prior on the m_i only leads to at most a 3% degradation in cosmological parameters. Completely relaxing shear bias priors only leads to a 25% degradation at most.

In the absence of shear priors, the self-calibration of the shear is better than 2% for cosmic shear alone and better than 1.5% for LSST, in most of the redshift range. This is shown in Fig. 5, left panel.

Note that all these results assumed photo-z uncertainties as in Table I. We vary these photo-z assumptions in Sec. IV B. Note also that this self-calibration from LSST alone relies on the comparison between large scales and small scales. It is therefore somewhat susceptible to nonlinearities and baryonic effects in the matter power spectrum.

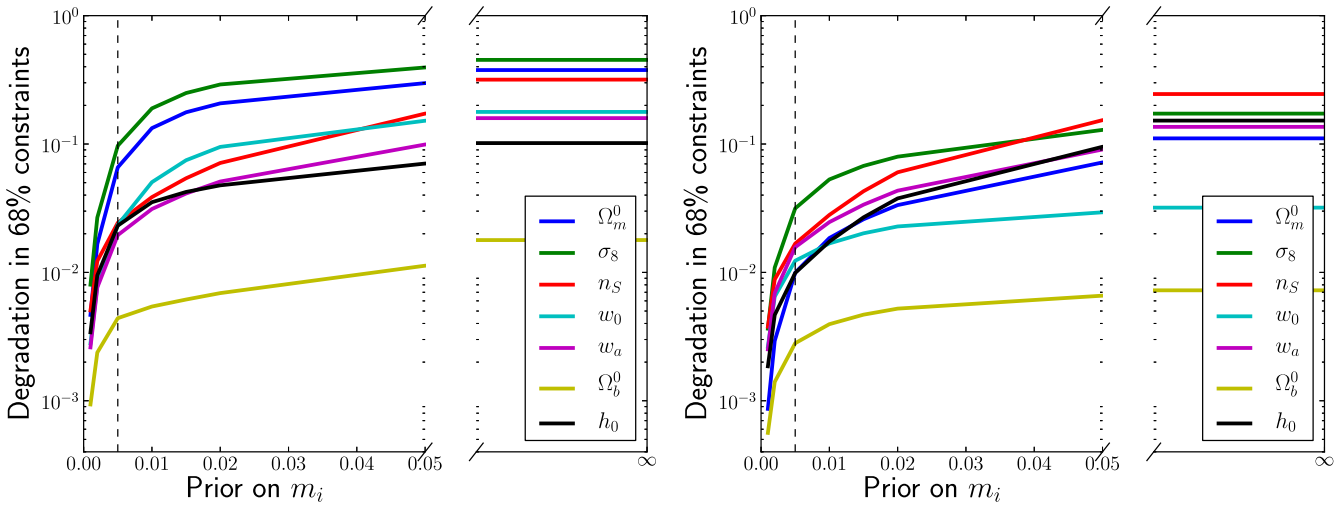

FIG. 4. Degradation in cosmological parameter constraints, relative to a perfect shear calibration, as a function of shear bias prior. A shear bias prior of 0 corresponds to perfect shear calibration and to 0 degradation in cosmological constraints. A shear bias prior of ∞ amounts to completely relaxing any shear prior, i.e., self-calibrating the shear from the data. A degradation of 1 corresponds to a 100% increase in cosmological parameter error bars, compared to the case with perfect shear calibration. Left panel: Degradation in cosmological parameter constraints for cosmic shear alone, from LSST. Right panel: Degradation in cosmological parameter constraints for LSST, when combining cosmic shear, galaxy-galaxy lensing, and clustering.

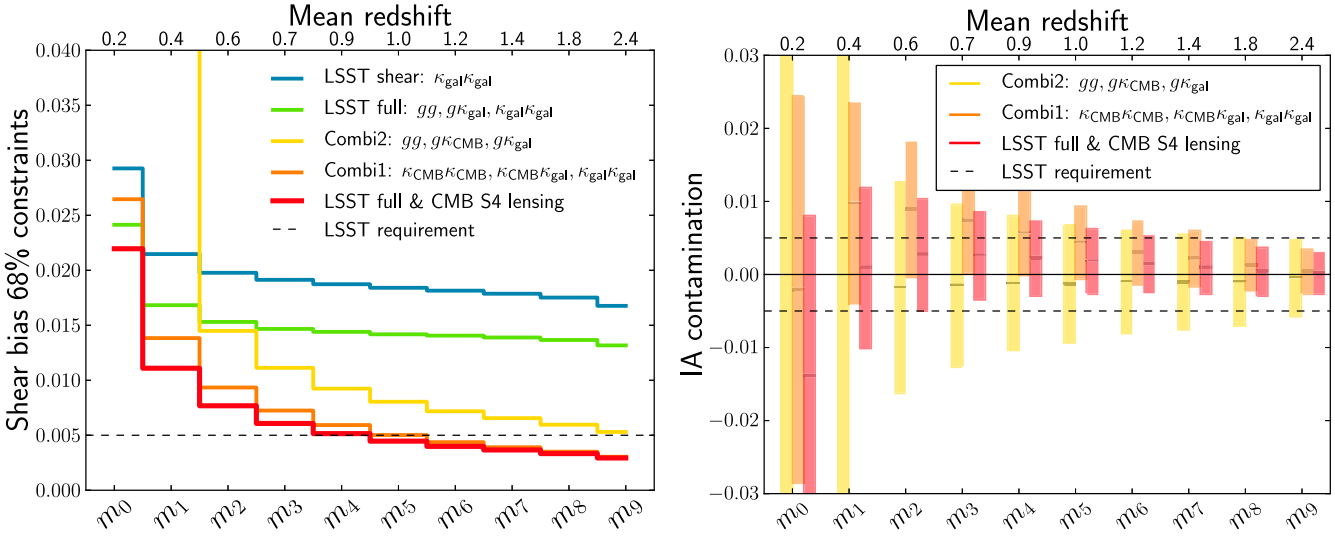

FIG. 5. Left panel: 68% confidence constraints on the shear biases m_i for LSST, when self-calibrating them with LSST cosmic shear alone (blue), LSST full (i.e., clustering, galaxy-galaxy lensing, and cosmic shear; green), combination 1 (orange), combination 2 (yellow), and the full LSST and CMB S4 lensing (red). The self-calibration works down to the level of LSST requirements (dashed lines) for the highest redshift bins, where shear calibration is otherwise most difficult. We stress that all the solid lines correspond to self-calibration from the data alone, without relying on image simulations. Calibration from image simulations is expected to meet the LSST requirements, and CMB lensing will thus provide a valuable consistency check for building confidence in the results from LSST. Right panel: Impact of unaccounted intrinsic alignments of early-type galaxies (see Sec. II D). The lines show the bias in the self-calibrated value of m_i, and the colored bands show the 68% confidence constraints, corresponding to the curves in the left panel. Intrinsic alignments produce a bias in the shear calibration, but not beyond the 68% confidence region.

B. Approaching or surpassing the LSST requirements with CMB S4

Having examined the impact of shear calibration on cosmology for LSST alone, we now add CMB lensing data from CMB S4. We wish to identify the combination of observables that best constrains the shear biases m_i, taking into account statistical and systematic errors. To do so, we consider separately combinations 1 and 2 [Eq. (10)], as well as all the two-point functions of LSST and CMB S4 lensing ["full LSST & CMB S4 lensing," Eq. (8)]. We compare the resulting level of shear self-calibration to the case of LSST cosmic shear alone ("LSST shear"), and the combination of all two-point functions from LSST ("LSST full," including clustering, galaxy-galaxy lensing, and cosmic shear). The shear bias constraints are shown in Fig. 5.

As shown in Table II, the statistical SNR is higher for combination 1 than combination 2, which explains the slightly better constraints on the shear bias seen in Fig. 5. As explained earlier, this is a consequence of our conservative tracer sample. We also notice that the shear biases m_0 and m_1 of the first two tomographic bins are not constrained by combination 2. This is because we only include tracer-lensing correlations when the entire source bin is at a higher redshift than the tracer bin.

In the case of the full LSST and CMB S4 lensing, we find that the shear biases are constrained down to 0.3% for the highest redshift bins and 2% for the lowest redshift bins. For higher source bins, the lensing efficiency kernels for $\kappa_{\rm gal}$ and $\kappa_{\rm CMB}$ overlap more, leading to a larger signal, correlation coefficient, and signal to noise (the SNR for $\kappa_{\rm gal}\kappa_{\rm CMB}$ goes from 15 for the lowest redshift bin to 330 for the highest redshift bin). Thus, CMB lensing from CMB S4 can approach and surpass the LSST requirements for shear calibration for most of the tomographic bins.

We assess the impact of intrinsic alignments by including our IA model into the data vector and not accounting for it in the fit. This allows us to estimate the size of the bias due to IA. Again, we do not account for catastrophic failures in the photo-z and restrict ourselves to Gaussian photo-z uncertainties. The right panel of Fig. 5 shows that combination 2 is less affected by intrinsic alignments than combination 1. This was expected since combination 2 involves tracer-lensing correlations: It is completely exempt of IA in the case of perfect photo-z, and little affected in the case of Gaussian photo-z. Furthermore, we selected a very conservative tracer sample, for which excellent photo-z should be achievable. So combination 2 should be very robust to intrinsic alignment contamination. In contrast, shear tomography is affected by the so-called GI term for the interbin correlations and by the II term for the bin autocorrelations. Similarly, galaxy lensing-CMB lensing is affected by the GI term [102–105]. This contamination is present even with perfect photo-z. However, IA only bias the shear calibration from combination 2 within the 68% confidence region, for our reasonable IA model. Furthermore, no IA mitigation technique was applied here, suggesting that this forecast is certainly conservative. This

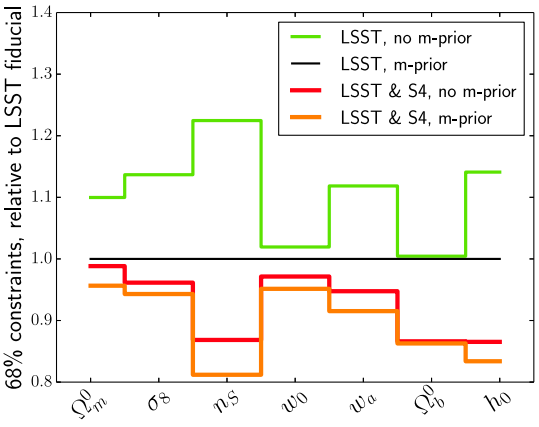

FIG. 6. Radius of the 68% confidence region for cosmological parameters, relative to the LSST fiducial forecast (with priors on the shear biases of 0.5%). The black line shows the fiducial LSST forecast, and the green line shows the degradation in cosmological constraints when relaxing the shear bias priors. For LSST alone, relaxing the shear bias priors degrades the cosmological parameters by up to ∼20%. The forecast for LSST and CMB S4 lensing is shown, without shear bias priors in red and with shear bias priors in orange. Thus, adding CMB lensing from S4 successfully replaces a prior on the shear bias (i.e., the red curve is below the black curve) and even surpasses the constraining power of LSST alone with shear priors at the level of the LSST requirements. Furthermore, the red and orange curves only differ by less than ∼5%, which means that the shear biases no longer play an important role, once CMB S4 lensing information is included. A contour plot of the cosmological constraints for LSST and CMB S4 is shown in Appendix A.

result was not obvious *a priori*. Indeed, at low redshift, IA contaminate the power spectrum by up to 5%–10% for $\kappa_{\rm gal}\kappa_{\rm gal}$ and $\kappa_{\rm gal}\kappa_{\rm CMB}$, in agreement with [25–28,102,103]. However, this bias becomes much smaller at higher redshift (the IA signal is roughly constant with redshift, while the lensing signal increases), and the higher redshift power spectra are measured with the best signal-to-noise ratio. As a result, the overall contamination due to IA is small. As described in Sec. II D, our model for the IA contamination extrapolates the observed IA strength of early-type galaxies to high redshifts but does not include the alignment of late-type galaxies, which has not been detected so far. Chisari *et al.* [103] find that late-type galaxy alignments, assuming an alignment strength consistent with the upper detection limits, may double the IA contamination to nontomographic $\kappa_{\rm gal}\kappa_{\rm CMB}$ correlations. It will be important to revisit this calculation as better models and observations of late-type galaxy alignments become available. The other key uncertainty of our IA model is the extrapolation of early-type IA contamination strength and galaxy luminosity function to the high redshifts relevant for LSST (see [85] for a discussion). Finally, when combining the full LSST and CMB S4, the overall impact of intrinsic alignments is negligible for the shear bias constraints.

In conclusion, we find that CMB lensing from CMB S4 can constrain the shear multiplicative bias down to or beyond LSST requirements, while jointly fitting for cosmology, galaxy biases, and photo-z uncertainties, and in the presence of reasonable intrinsic alignments. The method works best at higher redshift, where shear calibration is expected to otherwise be most difficult. This result is extremely encouraging and is an example of synergy between stage 4 surveys, where multiprobe analyses lead to a dramatic improvement in control over systematics. In Fig. 6, we show that including CMB lensing from CMB S4 can successfully replace a prior on the shear biases m_i, and it can even improve the cosmological constraints over LSST alone with realistic priors on m_i. This forecast is conservative, as we include the non-Gaussian covariances, discard the small scales in clustering and

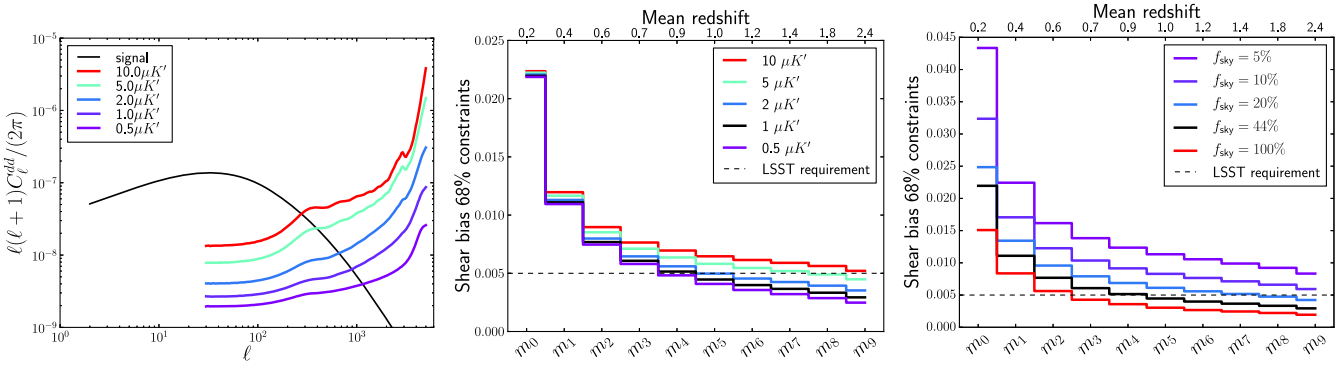

FIG. 7. Impact of CMB S4 sensitivity and area on the CMB lensing reconstruction noise and the shear calibration for LSST. Left panel: The CMB lensing power spectrum (black line) is compared to the reconstruction noise per ℓ mode (colored lines) for different values of sensitivity. When varying the sensitivity (left), we quote the white noise level in temperature and use a $\sqrt{2}$ times larger value for E and B polarizations. Center panel: The shear calibration level for the fiducial CMB S4 (black solid line) is compared to the one obtained for each value of the sensitivity. Right panel: The shear calibration level for the fiducial CMB S4 (black solid line) is compared to the one obtained for each value of sky area in common between LSST and CMB S4. The scaling with sky area is roughly $\propto 1/\sqrt{f_{\rm sky}}$. We can see that the dependence on noise (in $\mu K'$) is slower than the dependence on $\sqrt{f_{\rm sky}}$. Therefore, at fixed CMB S4 observing time, going wide is advantageous over going deep.

galaxy-galaxy lensing, and marginalize over galaxy bias, photo-z uncertainties, and cosmological parameters. It is also robust to intrinsic alignments and the assumptions for the CMB S4 specifications (see Sec. IV A) as well as photo-z priors (see Sec. IV B).

IV. IMPACT OF CMB S4 DESIGN AND LENSING SYSTEMATICS; APPLICATION TO SPACE-BASED LENSING SURVEYS

A. Importance of sensitivity and resolution for CMB S4

In this subsection, we quantify the impact of CMB S4 sensitivity, area, resolution, and component separation on shear calibration. In all cases, when one parameter is varied, the others remain fixed to their fiducial values from Fig. 1.

In Fig. 7, we show the reconstruction noise on the CMB lensing convergence $\kappa_{\rm CMB}$ as a function of sensitivity in temperature (assumed to be $\sqrt{2}$ times better than in polarization), and the corresponding constraints on shear biases m_i. The shear calibration improves slowly with sensitivity, by a factor of $\sim$2 when the noise varies from 10 to 0.5 $\mu K'$. This is understandable since the CMB lensing signal falls off quickly at high ℓ, and therefore a significant reduction in reconstruction noise is needed to image higher ℓ lensing modes. For the same reason, we expect iterative lensing reconstruction methods [67,68] to only improve shear calibration by a few tens of percent. We compare the effect of sensitivity to the importance of sky coverage in the same figure, and we find that at fixed CMB S4 observing time, going wide is advantageous over going deep.

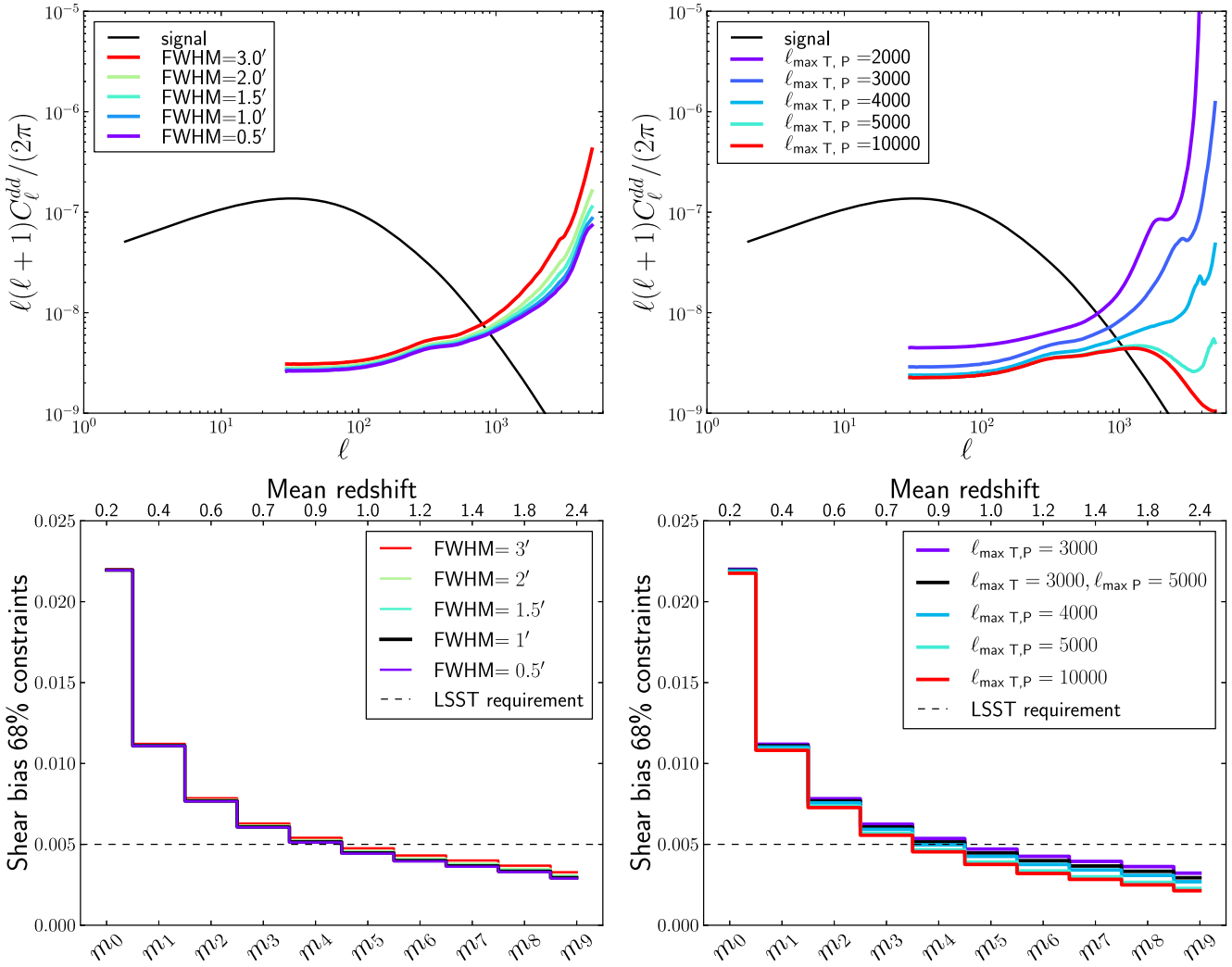

FIG. 8. Impact of CMB S4 resolution and foreground separation on the CMB lensing reconstruction noise and the shear calibration for LSST. Top row: The CMB lensing power spectrum (black line) is compared to the reconstruction noise per ℓ mode (colored lines) for different values of beam FWHM (left) and maximum multipole where a foreground-cleaned CMB map is available (right). When varying the maximum multipole (right), we assume $l_{\rm max\,T} = l_{\rm max\,P}$. Bottom row: The shear calibration level for the fiducial CMBS4 (black solid line) is compared to the one obtained for each variation (solid colored lines). The LSST requirement is shown as the black dashed lines. The shear calibration is relatively insensitive to the beam and maximum multipole available. This is encouraging, allowing conservative $\ell_{\rm max}$ cuts to be used, and it suggests that AdvACT and SPT-3G will already be useful for calibrating the shear from LSST.

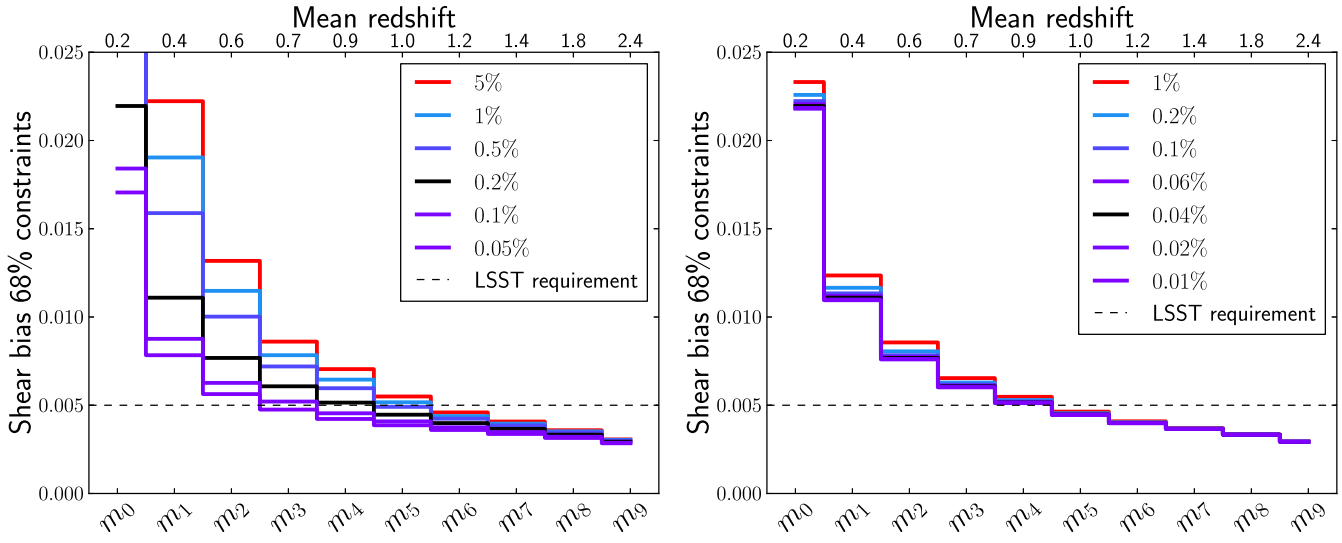

FIG. 9. Left panel: Level of shear calibration for LSST with CMB S4 lensing, when varying the source photo-z priors. The black line corresponds to the fiducial priors, and the colored lines are labeled with "$x\%$" such that the prior on $\Delta_{z,\mathrm{source},i}$ is Gauss(0, $x\%$) and the prior on $\sigma_{z,\mathrm{source}}/(1+z)$ is Gauss(0.05, $1.5\times x\%$). The dependence is more important at low redshift, where a fixed absolute change in z corresponds to a larger relative change in comoving distance. Right panel: Varying lens photo-z priors. Similarly to the left panel, the black line corresponds to the fiducial priors, and the colored lines are labeled with "$x\%$" such that the prior on $\Delta_{z,\mathrm{lens},i}$ is Gauss(0, $x\%$) and the prior on $\sigma_{z,\mathrm{lens}}/(1+z)$ is Gauss(0.01, $1.5\times x\%$). The shear calibration is almost completely insensitive to the lens photo-z priors.

In Fig. 8, we vary the beam FWHM (left) and maximum multipole included in the analysis $\ell_{\mathrm{max\ T,P}}$ (parametrizing the effectiveness of component separation; right). The bottom row of Fig. 8 shows the corresponding constraints on the shear biases. For our choice of fiducial ℓ limits ($\ell_{\mathrm{max}} = 3000$ for T; $\ell_{\mathrm{max}} = 5000$ for E, B), set by foreground cleaning, varying the beam FWHM between $0.5'$ and $3'$ basically has no impact on the shear calibration: A higher resolution experiment can image higher ℓ modes, but we are discarding these small scales to avoid foreground contamination.

More realistically, a higher resolution experiment might perform better at component separation and allow us to use higher temperature and polarization multipoles. However, for

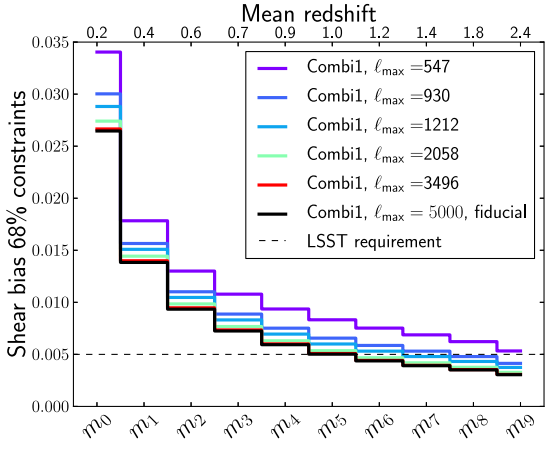

FIG. 10. In this figure, we vary the maximum multipole included in the lensing-lensing correlations and compare the resulting shear calibrations from combination 1 (i.e., $\kappa_{\mathrm{gal}}\kappa_{\mathrm{gal}}$, $\kappa_{\mathrm{gal}}\kappa_{\mathrm{CMB}}$, $\kappa_{\mathrm{CMB}}\kappa_{\mathrm{CMB}}$). Between $\ell_{\mathrm{max}} = 5,000$ and $\ell_{\mathrm{max}} = 930$, the shear calibration is only degraded by 10%–40%. Besides, the calibration from combination 2 (i.e., gg, $g\kappa_{\mathrm{gal}}$, $g\kappa_{\mathrm{CMB}}$; not shown in this figure) only uses lower multipoles ($\ell_{\mathrm{max}} = 420$, 714, 9390, 1212 for the four lens bins). As a result, the calibration from the full LSST and CMB S4 lensing is rather insensitive to the maximum multipole included, beyond ~1000. Therefore, it should be robust to uncertainties in nonlinearities and baryonic effects in the matter power spectrum.

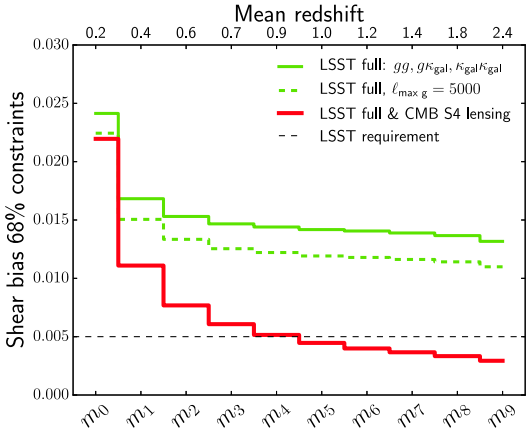

FIG. 11. The 68% confidence constraints on the shear biases m_i for LSST, when self-calibrating them with LSST alone (solid green), with LSST alone but extending the clustering and galaxy-lensing analyses to $\ell_{\mathrm{max}} = 5000$ (dashed green), and with the full combination of LSST and CMB S4 lensing (solid red). In the absence of CMB lensing information, even the very optimistic assumption of linear bias out to $\ell_{\mathrm{max}} = 5000$ (dashed green) does not reach the LSST requirements (dashed black). In contrast, adding CMB S4 lensing allows us to reach the required 0.5%.

our fiducial parameters, we find that varying $\ell_{\mathrm{max\,T,P}}$ between 2000 and 10000 only changes the shear calibration by about 25%.

This is encouraging and shows that upcoming third-generation experiments such as Advanced ACT (AdvACT, 1.4′ resolution, ∼10 $\mu K'$ sensitivity on half of the sky) [52] and SPT-3G (1′ resolution, 2.5 $\mu K'$ sensitivity on 2500 deg^2) [53] can already calibrate the shear from LSST. This calibration will be less precise than from CMB S4, but already at a useful level. The amount of overlap of AdvACT and SPT-3G with LSST may evolve in the future and will affect the shear calibration.

B. Sensitivity to photometric redshift uncertainties

In Sec. III B, we showed that CMB S4 lensing can calibrate the shear from LSST, assuming that the photometric redshift uncertainties are under control. In this subsection, we ask how crucial this assumption is. We therefore vary the priors on source and lens photo-z uncertainties and rerun our forecast. The left panel of Fig. 9 shows that the shear calibration is mildly dependent on the source photo-z uncertainties. The dependence is higher at low redshift, where a fixed change in redshift corresponds to a larger relative change in comoving distance. The right panel of Fig. 9 shows that the shear calibration is very insensitive to the lens photo-z uncertainties. This is in large part because most of the constraining power comes from autocorrelations and cross-correlations of the galaxy lensing and CMB lensing, which are not affected by the lens photo-z uncertainties.

These results are encouraging: They show that the shear calibration is robust to larger photometric redshift uncertainties. Note, however, that we have not taken into account catastrophic photo-z failures.

C. Robustness to nonlinearities and baryonic effects

As pointed out earlier, our clustering and galaxy-galaxy lensing only use large scales, $2\pi\chi(z_{\mathrm{mean}})/l > 10$ Mpc/h, which correspond to $\ell_{\mathrm{max}} = 420$, 714, 930, and 1212, respectively, for the four lens bins. Thus, combination 2 (i.e., gg, $g\kappa_{\mathrm{gal}}$, $g\kappa_{\mathrm{CMB}}$) is only sensitive to scales greater than

Euclid specifications	
Ω_s	15,000 deg^2
source distribution	$dn_{\mathrm{source}}/dz \propto z^\alpha e^{-(z/z_0)^\beta}$, $\alpha = 1.3, \beta = 1.5, z_0 = 0.65$, $n_{\mathrm{source}} = 30$ arcmin^{-2}, 10 bins, $\sigma_\epsilon = 0.26$
lens distribution	$dn_{\mathrm{lens}}/dz \propto \chi(z)^2/H(z)$, $n_{\mathrm{lens}} = 0.25$ arcmin^{-2}, 4 bins

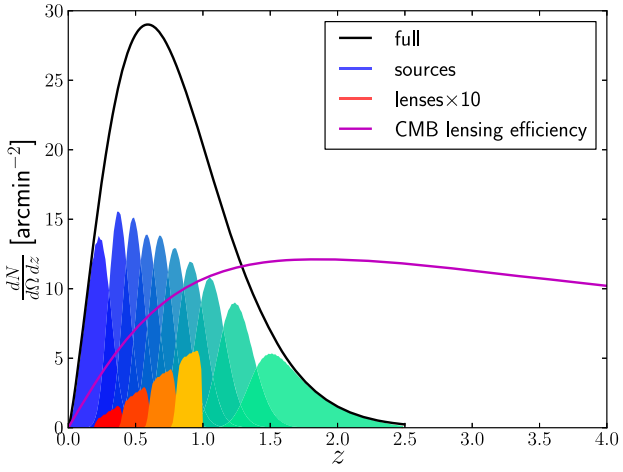

Euclid & CMB S4	SNR
Individual probes	
clustering (gg)	344
galaxy-galaxy lensing: $g\kappa_{\mathrm{gal}}$	230
galaxy-CMB lensing: $g\kappa_{\mathrm{CMB}}$	141
shear tomography: $\kappa_{\mathrm{gal}}\kappa_{\mathrm{gal}}$	375
CMB lensing auto: $\kappa_{\mathrm{CMB}}\kappa_{\mathrm{CMB}}$	366
galaxy lensing-CMB lensing: $\kappa_{\mathrm{gal}}\kappa_{\mathrm{CMB}}$	261
Combinations	
Euclid: $gg, g\kappa_{\mathrm{gal}}, \kappa_{\mathrm{gal}}\kappa_{\mathrm{gal}}$	486
Combination 1: $\kappa_{\mathrm{CMB}}\kappa_{\mathrm{CMB}}, \kappa_{\mathrm{CMB}}\kappa_{\mathrm{gal}}, \kappa_{\mathrm{gal}}\kappa_{\mathrm{gal}}$	510
Combination 2: $gg, g\kappa_{\mathrm{CMB}}, g\kappa_{\mathrm{gal}}$	364
Full: $gg, g\kappa_{\mathrm{CMB}}, g\kappa_{\mathrm{gal}}, \kappa_{\mathrm{CMB}}\kappa_{\mathrm{CMB}}, \kappa_{\mathrm{CMB}}\kappa_{\mathrm{gal}}, \kappa_{\mathrm{gal}}\kappa_{\mathrm{gal}}$	592

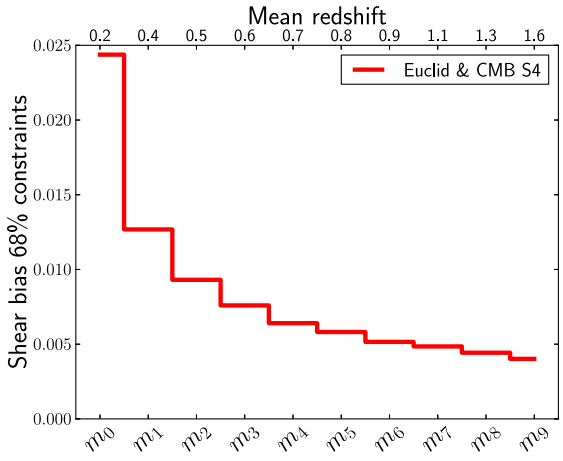

FIG. 12. Summary of the forecast for Euclid and CMB S4 lensing. The top left panel summarizes our assumptions for the Euclid survey. The top right panel displays the photo-z bins assumed for the lens and source samples. The bottom left panel summarizes the signal-to-noise ratios for the various probes and combinations. The bottom right panel shows the level of shear calibration in Euclid's ten source bins.

10 Mpc/h. This conservative cut makes linear biasing valid and avoids systematic errors from halo occupation modeling, nonlinearities, and baryonic effects in the matter power spectrum. As a result, the shear calibration from combination 2 (see Fig. 5) should be very robust to these effects.

On the other hand, combination 1 (i.e., $\kappa_{\rm gal}\kappa_{\rm gal}$, $\kappa_{\rm gal}\kappa_{\rm CMB}$, $\kappa_{\rm CMB}\kappa_{\rm CMB}$) uses lensing-lensing correlations. Because the lensing kernels extend to very low redshift, a fixed angular scale receives contributions from arbitrarily small scales. Furthermore, our fiducial forecast includes the modes of $\kappa_{\rm gal}$ and $\kappa_{\rm CMB}$ up to $\ell_{\rm max} = 5000$. Rigorously assessing the contamination from uncertainties in the matter power spectrum is beyond the scope of this paper (see [22] for details). However, this contamination is expected to be less important for small multipoles. We thus vary the maximum multipole $\ell_{\rm max}$ and show the impact on shear calibration from combination 1 in Fig. 10. The shear calibration from combination 1 is only degraded by 10%–40% when reducing $\ell_{\rm max}$ from 5000 to 930. The shear calibration from the full LSST and CMB S4 lensing is therefore even less affected. This is likely because at $\ell \gtrsim 1000$, both CMB and galaxy lensing stop being cosmic variance limited, and the relative uncertainty on the lensing-lensing power spectra starts growing.

In conclusion, the shear calibration is little affected by the maximum multipole included, beyond $\ell_{\rm max} \sim 1000$, which makes it robust to uncertainties in the modeling of nonlinearities and baryonic effects.

D. Optimistic modeling of galaxy bias does not replace CMB lensing

Throughout this paper, we make very conservative assumptions about the tracer sample, in terms of number density as well as the scales that we use. We restrict ourselves to large scales, where linear biasing is thought to be valid. One might wonder whether extending the analysis to smaller scales may improve the shear calibration, even without including CMB lensing, thus making the CMB lensing information unnecessary.

In this subsection, we show that this is not the case: We extend the clustering and galaxy-lensing analyses to $\ell_{\rm max} = 5000$ and show that the resulting shear self-calibration for LSST does not reach the LSST requirements, unless CMB

WFIRST specifications	
$\Omega_{\rm s}$	2,200 deg^2
source distribution	$dn_{\rm source}/dz \propto z^\alpha e^{-(z/z_0)^\beta}$, $\alpha = 1.27, \beta = 1.02, z_0 = 0.6$, $n_{\rm source} = 45$ arcmin^{-2}, 10 bins, $\sigma_\epsilon = 0.26$
lens distribution	$dn_{\rm lens}/dz \propto \chi(z)^2/H(z)$, $n_{\rm lens} = 0.25$ arcmin^{-2}, 4 bins

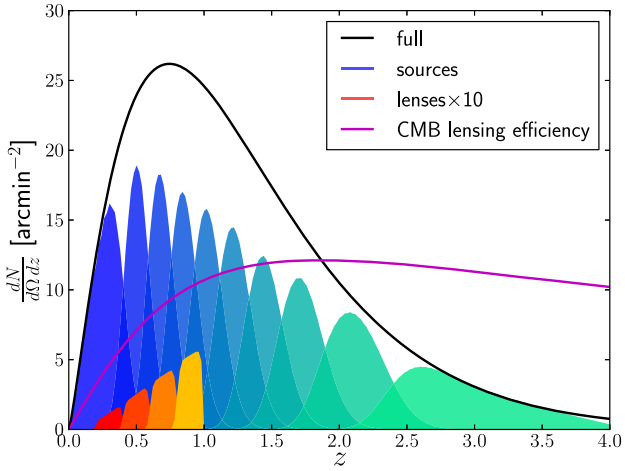

WFIRST & CMB S4	SNR
Individual probes	
clustering (gg)	131
galaxy-galaxy lensing: $g\kappa_{\rm gal}$	103
galaxy-CMB lensing: $g\kappa_{\rm CMB}$	54
shear tomography: $\kappa_{\rm gal}\kappa_{\rm gal}$	232
CMB lensing auto: $\kappa_{\rm CMB}\kappa_{\rm CMB}$	140
galaxy lensing-CMB lensing: $\kappa_{\rm gal}\kappa_{\rm CMB}$	154
Combinations	
WFIRST: $gg, g\kappa_{\rm gal}, \kappa_{\rm gal}\kappa_{\rm gal}$	254
Combination 1: $\kappa_{\rm CMB}\kappa_{\rm CMB}, \kappa_{\rm CMB}\kappa_{\rm gal}, \kappa_{\rm gal}\kappa_{\rm gal}$	262
Combination 2: $gg, g\kappa_{\rm CMB}, g\kappa_{\rm gal}$	142
Full: $gg, g\kappa_{\rm CMB}, g\kappa_{\rm gal}, \kappa_{\rm CMB}\kappa_{\rm CMB}, \kappa_{\rm CMB}\kappa_{\rm gal}, \kappa_{\rm gal}\kappa_{\rm gal}$	282

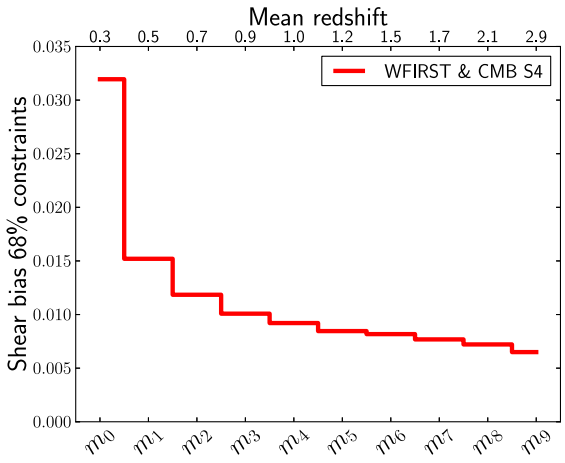

FIG. 13. Summary of the forecast for WFIRST and CMB S4 lensing. The top left panel summarizes our assumptions for the WFIRST survey. The top right panel displays the photo-z bins assumed for the lens and source samples. The bottom left panel summarizes the signal-to-noise ratios for the various probes and combinations. The bottom right panel shows the level of shear calibration in WFIRST's ten source bins.

lensing is included. The multipole of $\ell_{\rm max} = 5000$ corresponds to very small scales, where a halo occupation distribution would typically be necessary. However, we intentionally keep the linear biasing assumption to show that CMB lensing is useful, even in this very optimistic scenario.

As shown in Fig. 11, extending to $\ell_{\rm max} = 5000$ only improves the LSST-only shear calibration from 1.5% to 1.2%, short of the LSST requirement of 0.5%.

E. Application to space-based lensing surveys: Euclid and WFIRST

In this subsection, we reproduce our main forecast on shear calibration for Euclid and WFIRST. Our assumptions and results for Euclid follow [10,106] and are summarized in Fig. 12. In particular, we assume a survey area of $15,000$ deg^2 with 30 source galaxies per arcmin^2. For WFIRST, we follow [11] and present assumptions and results in Fig. 13. We assume a 2200 deg^2 survey area with 45 sources/arcmin^2. In both cases, we use ten tomographic source bins, and the same redMaGiC-like lens sample as for LSST, with four lens bins. For all cosmological and nuisance parameters, including photo-z uncertainties, we use the same priors as for LSST (see Table I).

As shown in Figs. 12 and 13, CMB lensing from S4 can calibrate the shear for the ten Euclid source bins down to 0.4%–2.4%, and for the ten WFIRST source bins down to 0.6%–3.2%. Note that the exact requirements for shear calibration for Euclid and WFIRST may differ from each other and from LSST. Furthermore, the exact redshift distributions and survey parameters may evolve in the future, in particular, for WFIRST. Nevertheless, these results are highly encouraging.

V. CONCLUSION

In this study, we answer the following questions: Can CMB lensing calibrate the shear bias down to a useful accuracy, competitive with image simulations and comparable with the LSST requirements? Is this possible while marginalizing over cosmological and nuisance parameters? How robust is this calibration to intrinsic alignments, photo-z uncertainties, nonlinear and baryonic effects, and assumptions on the CMB S4 experiment? To do so, we extend the COSMOLIKE framework to include CMB lensing. We jointly analyze all the two-point correlation functions of galaxy positions, shear, and CMB lensing convergence. We include the non-Gaussian covariances and explore the posterior distribution with MCMC sampling and the Fisher approximation. Our forecasts simultaneously vary cosmological parameters, galaxy biases, photo-z uncertainties for each source and lens bin, and shear calibration for each source bin. We make conservative choices of galaxy samples and scales. We therefore expect our forecast to be realistic and robust.

We show that CMB lensing from S4 can calibrate the shear multiplicative biases for LSST down to 0.3%–2% in ten tomographic bins, surpassing the LSST requirements of ~0.5% in most of the redshift range. This method performs best in the highest redshift bins, where shear calibration is otherwise most challenging. We show a shear calibration of 0.4%–2.4% for Euclid's ten tomographic source bins and 0.6%–3.2% for WFIRST's ten bins. For a reasonable level of intrinsic alignments and Gaussian photo-z uncertainties, the shear calibration from CMB S4 lensing is only biased at a fraction of the statistical uncertainty. This shear calibration is sensitive to the noise level in CMB S4 maps but insensitive to the beam and maximum multipole at which component separation is performed, within sensible values. Thus, stage 3 CMB surveys such as AdvACT and SPT-3G, as well as the Simons Observatory, will already provide a meaningful shear calibration. It is mildly dependent on the photo-z priors for Gaussian photo-z errors, and on the maximum multipole included in the analysis, beyond $\ell_{\rm max} \sim 1000$. We did not consider explicitly photo-z outliers [72] or potential biases in the CMB lensing reconstruction [94,95].

In conclusion, we find that shear calibration from CMB lensing will be possible at a level competitive with or even exceeding the LSST requirements. This method is a powerful alternative to simulation-based calibration techniques, because it relies on the data directly. In the systematics-limited era of stage 4 weak lensing surveys, this method will provide redundancy and serve as a cross-check, in order to reliably measure the properties of dark energy, the neutrino masses, and possible modifications to general relativity.

ACKNOWLEDGMENTS

We thank Patricia Burchat, Scott Dodelson, Jo Dunkley, Simone Ferraro, Colin Hill, Gil Holder, Bhuvnesh Jain, Alexie Leauthaud, Jia Liu, Mathew Madhavacheril, Rachel Mandelbaum, Roland de Putter, Uroš Seljak, Blake Sherwin, Sukhdeep Singh, and Martin White for useful discussions about shear calibration with CMB lensing. We thank Bob Armstrong, Eric Huff, and Peter Melchior for useful discussions about shear systematics. We thank Elisa Chisari, Rachel Mandelbaum, and Sukhdeep Singh for useful discussions about intrinsic alignments. We thank Scott Dodelson, Jo Dunkley, Simone Ferraro, Bhuvnesh Jain, Rachel Mandelbaum, Peter Melchior, and Sukhdeep Singh for feedback on an earlier version of this paper. We thank the referee for useful comments. Numerical calculations in this work were carried out using computational resources supported by the Princeton Institute of Computational Science and Engineering. We thank Jim Stone and the Computational Science and Engineering Support for access to these resources and invaluable help. E. S. was supported, in part, by a Jet Propulsion Laboratory (JPL) Strategic Universities Research Partnership grant. J. R., T. E., and H. M. were supported by JPL, which is operated by Caltech under a contract from National Aeronautics and Space Administration (NASA). Part of the research described in this paper was carried out at the JPL, California Institute of Technology, under a contract with the NASA.

APPENDIX A: COSMOLOGICAL PARAMETER DEPENDENCE

In this appendix, we show the dependences of the various two-point correlation functions on the cosmological parameters (Fig. 14). These figures show the logarithmic derivative of the observables with respect to the parameters varied. Together with the covariance matrix in Fig. 3, they are the key ingredients needed to perform a Fisher forecast. The width of the lines or bands displayed corresponds to the range of variation across tomographic bins.

These figures give intuition on the scaling of observables with parameters and can be interpreted as follows.

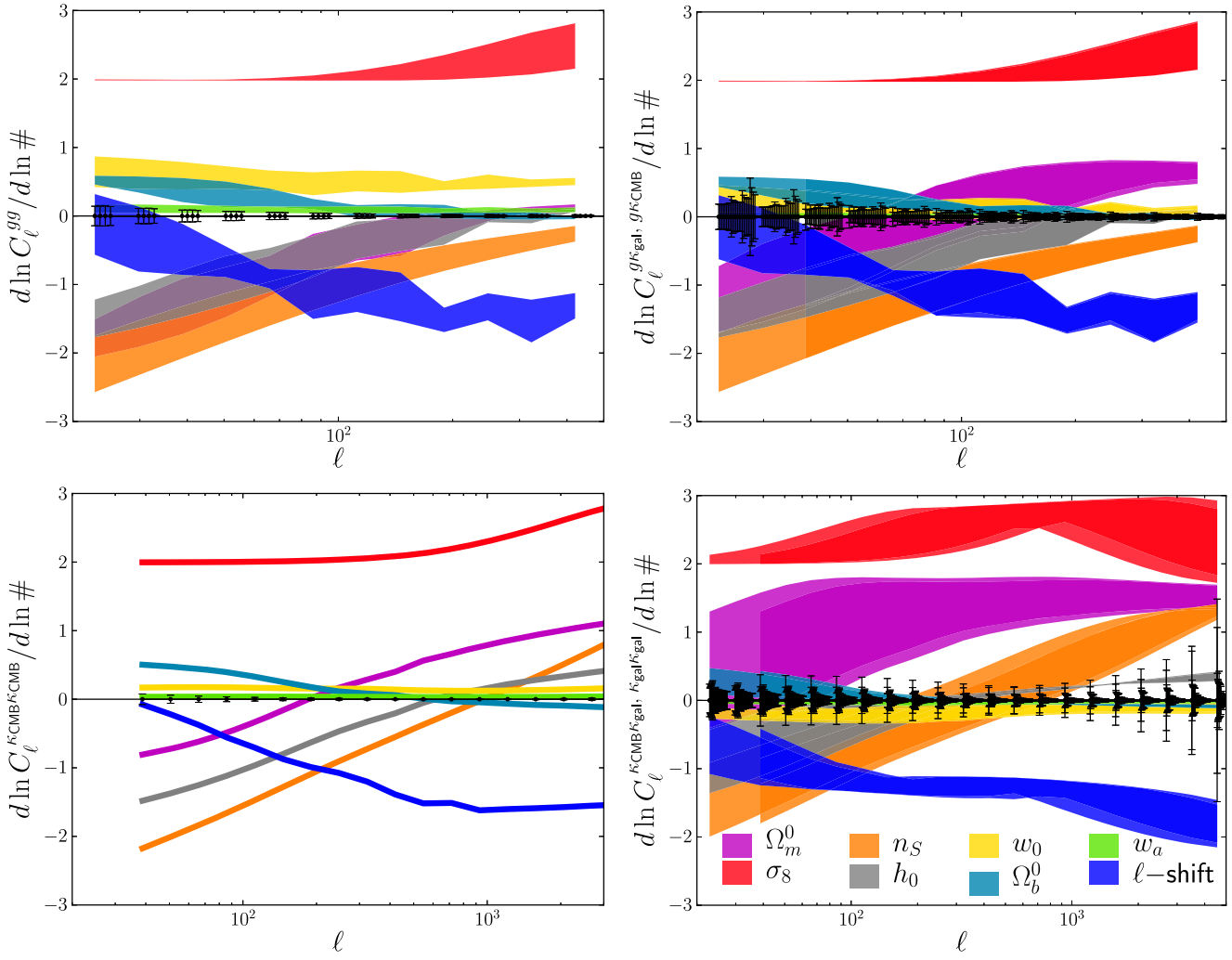

FIG. 14. Logarithmic derivatives of observables with respect to cosmological parameters, showing the scalings of observables with parameters. Together with the covariance matrix in Fig. 3, these plots visualize the information required for the Fisher forecast. They give intuition on the parameter dependences and degeneracies. Top left: Clustering. Top right: Galaxy-CMB lensing and galaxy-galaxy lensing. Bottom left: CMB lensing auto-spectrum. Bottom right: Cosmic shear and galaxy lensing-CMB lensing. The width of the lines or bands corresponds to the range of variation across tomographic bins. On these plots, a high absolute value corresponds to a strong parameter dependence. A positive value corresponds to an observable growing with the parameter. A horizontal curve corresponds to a multiplicative factor, and a slanted curve corresponds to a tilt in the observable, when the parameter is varied. Two curves that are identical modulo a multiplicative factor correspond to a perfect degeneracy between parameters. For example, all observables scale roughly as $\propto\sigma_8^2$ in the linear regime and σ_8^3 in the nonlinear regime. The parameter Ω_m^0 typically produces a tilt and is strongly degenerate with h_0 for clustering (top left panel).

A 1% change in parameter p produces a $\frac{d\ln\mathcal{O}}{d\ln p}\%$ change in observable $\mathcal{O}$. Therefore, observable $\mathcal{O}$ grows with parameter p if $\frac{d\ln\mathcal{O}}{d\ln p} \geq 0$. Observable $\mathcal{O}$ is strongly dependent on parameter p if $|\frac{d\ln\mathcal{O}}{d\ln p}|$ is large. In this case, a measurement of $\mathcal{O}$ will be very constraining for parameter p.

If $\frac{d\ln\mathcal{O}}{d\ln p}$ is independent of ℓ, then the parameter p simply acts as a multiplicative factor with $\mathcal{O} \propto p^{\frac{d\ln\mathcal{O}}{d\ln p}}$. For example, as seen in Fig. 14, all observables roughly satisfy $\frac{d\ln\mathcal{O}}{d\ln\sigma_8} = 2$, i.e., $\mathcal{O} \propto \sigma_8^2$, in the linear regime and

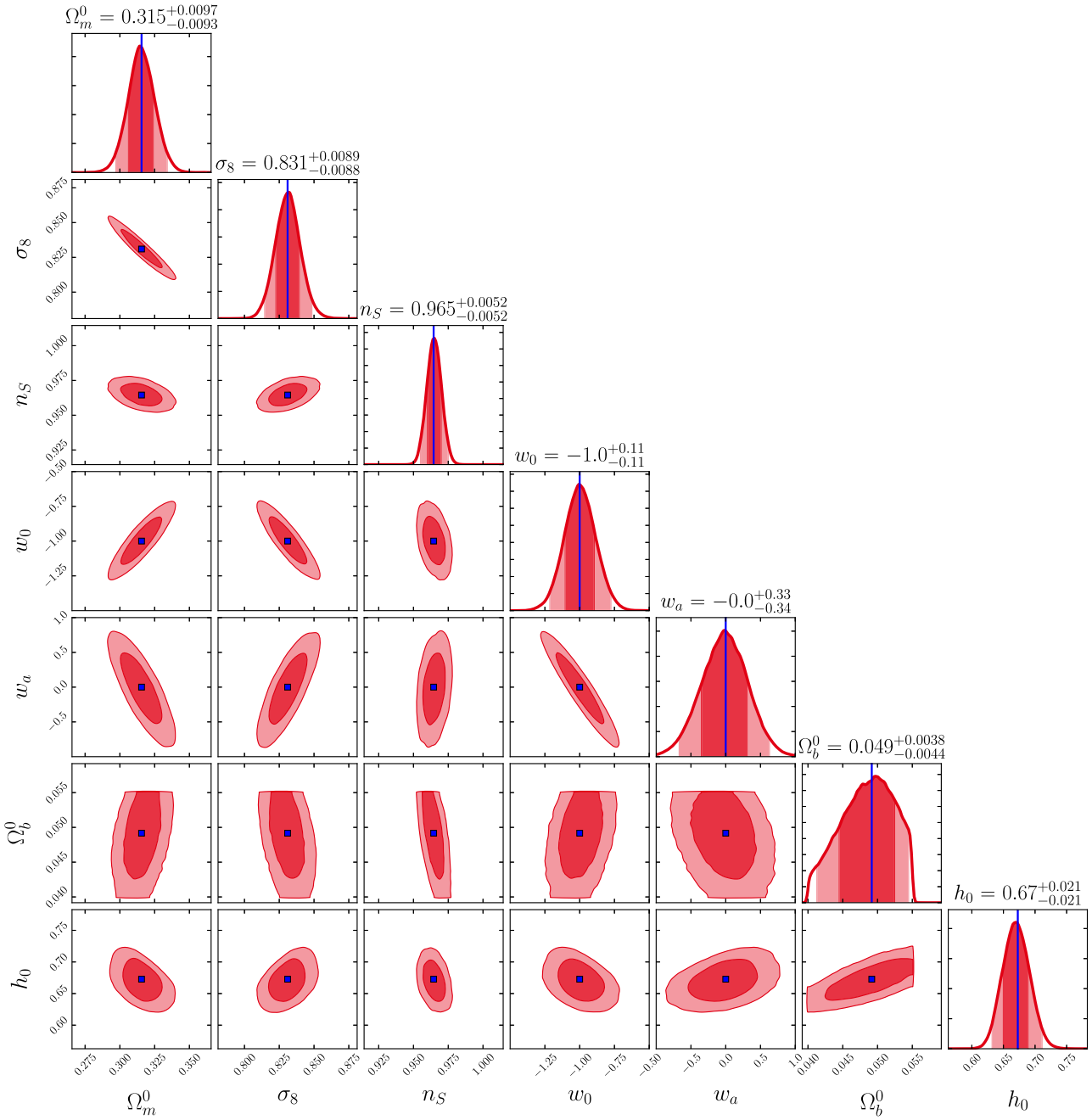

FIG. 15. Cosmological constraints from LSST and CMB S4 lensing. We marginalize over all the nuisance parameters, completely relaxing the priors on shear biases. The red zones indicate the 68% and 95% confidence regions. Striking features are the negative correlations for $\Omega_{\rm m}^0 - \sigma_8$, $\sigma_8 - w_0$, $w_0 - w_{\rm a}$ and the positive correlations for $\Omega_{\rm m}^0 - w_0$, $h_0 - \Omega_{\rm b}^0$, which can be understood in light of Fig. 14. The irregular shape of the confidence region for $\Omega_{\rm b}^0$ is a consequence of the flat prior imposed and the poor constraining power of the data for this parameter.

$\frac{d\ln\mathcal{O}}{d\ln\sigma_8} = 3$, i.e., $\mathcal{O} \propto \sigma_8^3$, in the nonlinear regime. If the curve of $\frac{d\ln\mathcal{O}}{d\ln p}$ as a function of ℓ is slanted, it means that the parameter p produces a tilt on $\mathcal{O}$. This is typically the case for Ω_m^0.

This figure also allows us to visualize parameter degeneracies and covariances. If two curves $\frac{d\ln\mathcal{O}}{d\ln p_1}(\ell)$ and $\frac{d\ln\mathcal{O}}{d\ln p_2}(\ell)$ are identical modulo a multiplicative factor, then the parameters p_1 and p_2 are perfectly degenerate. If these two curves are only similar modulo a multiplicative factor (where "similarity" depends on the covariance matrix), then the parameters p_1 and p_2 are partially degenerate and have a nonzero covariance.

Figure 15 shows the confidence regions for the seven cosmological parameters varied in our analysis. The negative correlations for $\Omega_{\rm m}^0 - \sigma_8$, $\sigma_8 - w_0$, $w_0 - w_{\rm a}$ and the positive correlations for $\Omega_{\rm m}^0 - w_0$, $h_0 - \Omega_{\rm b}^0$ can be understood in light of Fig. 14.

APPENDIX B: CONVERGENCE OF THE MCMC CHAINS; VALIDATION OF THE FISHER APPROXIMATION

In this appendix, we show the state of convergence of the MCMC chains and the agreement with the Fisher approximation. Figure 16 shows that Fisher and MCMC forecasts agree to better than 5% for all shear biases.

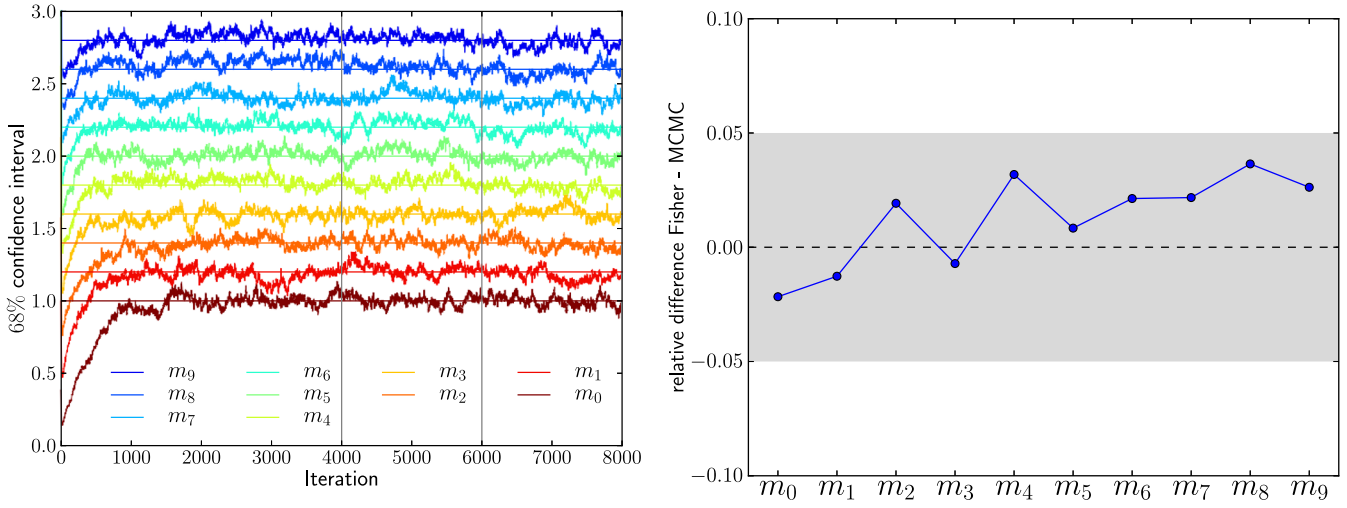

FIG. 16. Left panel: At each of the 8000 iterations, the radius of the 68% confidence interval for the shear biases is estimated from the 512 walkers at that same iteration and shown on this plot, normalized to the final quoted value and offset for clarity. The final quoted value is obtained by combining the last 4000 iterations. When comparing the estimated values from iterations 4000–6000 and 6000–8000, they differ by $\sqrt{2} \times (0.3\%\text{to}5\%)$. Right panel: Relative difference between Fisher approximation and MCMC result for the 68% confidence radius of the shear biases. The agreement is better than 5%, which implies a corresponding convergence of the MCMC chains, and the near-Gaussianity of the posterior distribution for the shear biases.

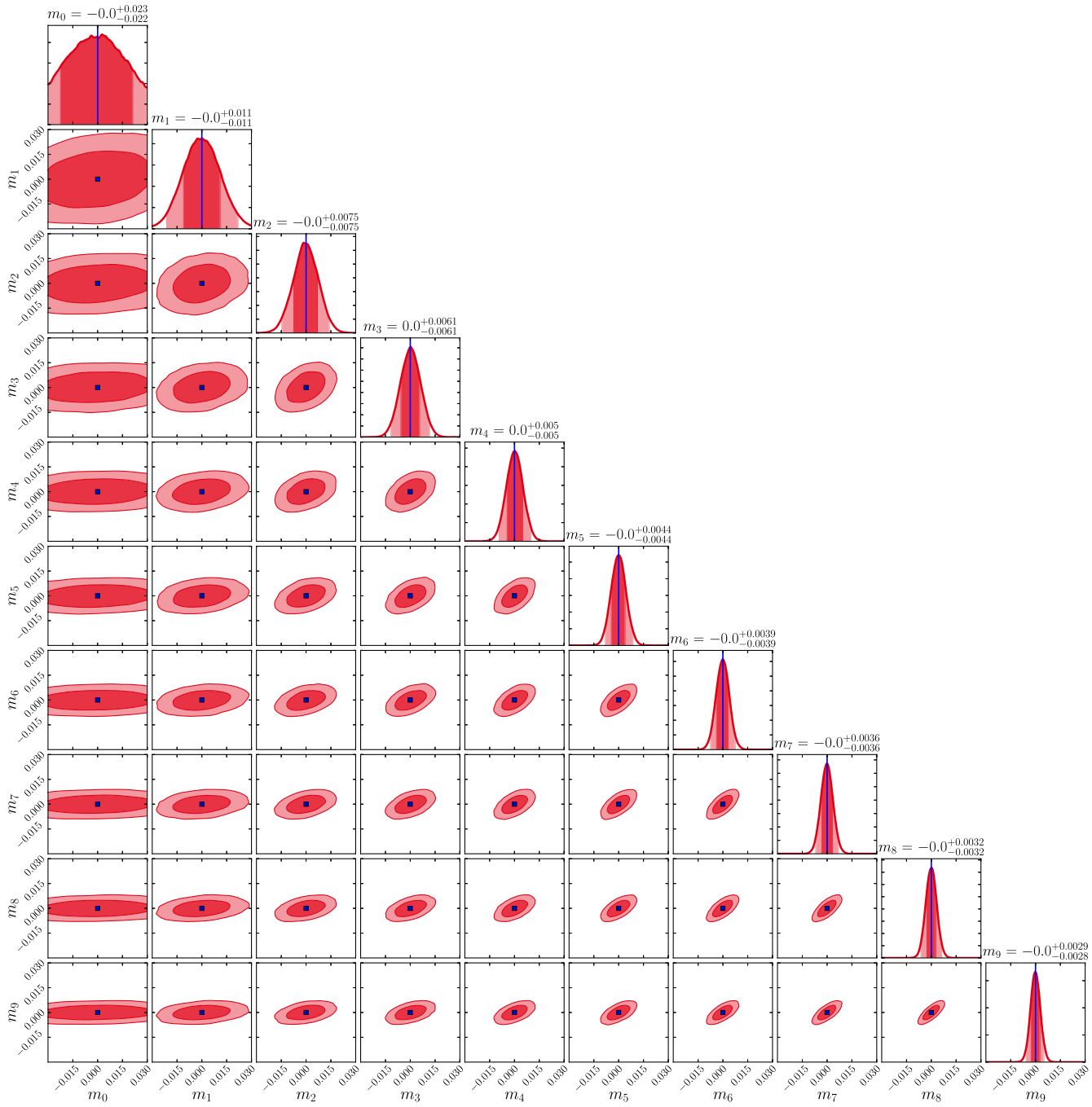

FIG. 17. Self-calibration of the shear biases from LSST and CMB S4 lensing. We marginalize over all the nuisance parameters, completely relaxing the priors on shear biases. The red zones indicate the 68% and 95% confidence regions. The posterior distributions are visually close to Gaussian, which explains the validity of the Fisher approximation shown in Fig. 16.

This good agreement is the result of two effects. First, it indicates convergence of the MCMC chains, which is not trivial given that we are jointly fitting 37 parameters. Second, it indicates that the posterior distribution for the shear biases is close to Gaussian. This was not obvious *a priori*, and it is in agreement with [107]. We show in Fig. 17 that the posterior is indeed close to Gaussian for the shear biases.

[1] See http://www.astro-wise.org/projects/KIDS.
[2] See http://www.darkenergysurvey.org.
[3] The Dark Energy Survey Collaboration, arXiv:astro-ph/0510346.
[4] See http://www.naoj.org/Projects/HSC/index.html.
[5] S. Miyazaki, Y. Komiyama, H. Nakaya, Y. Doi, H. Furusawa, P. Gillingham, Y. Kamata, K. Takeshi, and K. Nariai, Proc. SPIE Int. Soc. Opt. Eng. **6269**, 62690B (2006).
[6] See http://sumire.ipmu.jp/en/2652.
[7] M. Takada, R. Ellis, M. Chiba, J. E. Greene, H. Aihara, N. Arimoto, K. Bundy, J. Cohen, O. Doré, G. Graves *et al.*, Publ. Astron. Soc. Jpn. **66**, R1 (2014).
[8] See http://desi.lbl.gov.
[9] P. A. Abell, J. Allison, S. F. Anderson, J. R. Andrew, J. R. P. Angel, L. Armus, D. Arnett, S. J. Asztalos, T. S. Axelrod *et al.* (LSST Science Collaboration), arXiv:0912.0201.
[10] R. Laureijs, J. Amiaux, S. Arduini, J. Augueres, J. Brinchmann, R. Cole, M. Cropper, C. Dabin, L. Duvet, A. Ealet *et al.*, arXiv:1110.3193.
[11] D. Spergel, N. Gehrels, J. Breckinridge, M. Donahue, A. Dressler, B. S. Gaudi, T. Greene, O. Guyon, C. Hirata, J. Kalirai *et al.*, arXiv:1305.5425.
[12] D. H. Weinberg, M. J. Mortonson, D. J. Eisenstein, C. Hirata, A. G. Riess, and E. Rozo, Phys. Rep. **530**, 87 (2013).
[13] A. Albrecht, G. Bernstein, R. Cahn, W. L. Freedman, J. Hewitt, W. Hu, J. Huth, M. Kamionkowski, E. W. Kolb, L. Knox *et al.*, arXiv:astro-ph/0609591.
[14] D. Huterer, M. Takada, G. Bernstein, and B. Jain, Mon. Not. R. Astron. Soc. **366**, 101 (2006).
[15] Z. Ma and G. Bernstein, Astrophys. J. **682**, 39 (2008).
[16] D. H. Rudd, A. R. Zentner, and A. V. Kravtsov, Astrophys. J. **672**, 19 (2008).
[17] A. R. Zentner, D. H. Rudd, and W. Hu, Phys. Rev. D **77**, 043507 (2008).
[18] T. Eifler, Mon. Not. R. Astron. Soc. **418**, 536 (2011).
[19] M. P. van Daalen, J. Schaye, C. M. Booth, and C. D. Vecchia, Mon. Not. R. Astron. Soc. **415**, 3649 (2011).
[20] M. P. van Daalen, J. Schaye, I. G. McCarthy, C. M. Booth, and C. D. Vecchia, Mon. Not. R. Astron. Soc. **440**, 2997 (2014).
[21] M. Velliscig, M. P. van Daalen, J. Schaye, I. G. McCarthy, M. Cacciato, A. M. C. Le Brun, and C. D. Vecchia, Mon. Not. R. Astron. Soc. **442**, 2641 (2014).
[22] T. Eifler, E. Krause, S. Dodelson, A. R. Zentner, A. P. Hearin, and N. Y. Gnedin, Mon. Not. R. Astron. Soc. **454**, 2451 (2015).
[23] K. Osato, M. Shirasaki, and N. Yoshida, Astrophys. J. **806**, 186 (2015).
[24] W. A. Hellwing, M. Schaller, C. S. Frenk, T. Theuns, J. Schaye, R. G. Bower, and R. A. Crain, Mon. Not. R. Astron. Soc. **461**, L11 (2016).
[25] A. Kiessling, M. Cacciato, B. Joachimi, D. Kirk, T. D. Kitching, A. Leonard, R. Mandelbaum, B. M. Schäfer, C. Sifón, M. L. Brown, and A. Rassat, Space Sci. Rev. **193**, 67 (2015).
[26] D. Kirk, M. L. Brown, H. Hoekstra, B. Joachimi, T. D. Kitching, R. Mandelbaum, C. Sifón, M. Cacciato, A. Choi, A. Kiessling, A. Leonard, A. Rassat, and B. M. Schäfer, Space Sci. Rev. **193**, 139 (2015).
[27] B. Joachimi, M. Cacciato, T. D. Kitching, A. Leonard, R. Mandelbaum, B. M. Schäfer, C. Sifón, H. Hoekstra, A. Kiessling, D. Kirk, and A. Rassat, Space Sci. Rev. **193**, 1 (2015).
[28] M. A. Troxel and M. Ishak, Phys. Rep. **558**, 1 (2015).
[29] R. Massey, H. Hoekstra, T. Kitching, J. Rhodes, M. Cropper, J. Amiaux, D. Harvey, Y. Mellier, M. Meneghetti, L. Miller *et al.*, Mon. Not. R. Astron. Soc. **429**, 661 (2013).
[30] M. Jarvis, E. Sheldon, J. Zuntz, T. Kacprzak, S. L. Bridle, A. Amara, R. Armstrong, M. R. Becker, G. M. Bernstein, and C. Bonnett, Mon. Not. R. Astron. Soc. **460**, 2245 (2016).
[31] I. Fenech Conti, R. Herbonnet, H. Hoekstra, J. Merten, L. Miller, and M. Viola, arXiv:1606.05337 [Mon. Not. R. Astron. Soc. (to be published)].
[32] R. Mandelbaum, B. Rowe, R. Armstrong, D. Bard, E. Bertin, J. Bosch, D. Boutigny, F. Courbin, W. A. Dawson, A. Donnarumma *et al.*, Mon. Not. R. Astron. Soc. **450**, 2963 (2015).
[33] M. Zaldarriaga and U. Seljak, Phys. Rev. D **59**, 123507 (1999).
[34] W. Hu and T. Okamoto, Astrophys. J. **574**, 566 (2002).
[35] T. Okamoto and W. Hu, Phys. Rev. D **67**, 083002 (2003).
[36] A. Vallinotto, Astrophys. J. **759**, 32 (2012).
[37] A. Vallinotto, Astrophys. J. **778**, 108 (2013).
[38] S. Das, J. Errard, and D. Spergel, arXiv:1311.2338.
[39] K. M. Smith, O. Zahn, and O. Doré, Phys. Rev. D **76**, 043510 (2007).
[40] C. M. Hirata, S. Ho, N. Padmanabhan, U. Seljak, and N. A. Bahcall, Phys. Rev. D **78**, 043520 (2008).
[41] S. Das, B. D. Sherwin, P. Aguirre, J. W. Appel, J. R. Bond, C. S. Carvalho, M. J. Devlin, J. Dunkley, R. Dünner, T. Essinger-Hileman *et al.*, Phys. Rev. Lett. **107**, 021301 (2011).
[42] S. Das, T. Louis, M. R. Nolta, G. E. Addison, E. S. Battistelli, J. R. Bond, E. Calabrese, D. Crichton, M. J. Devlin, S. Dicker *et al.*, J. Cosmol. Astropart. Phys. 04 (2014) 014.
[43] M. Madhavacheril, N. Sehgal, R. Allison, N. Battaglia, J. R. Bond, E. Calabrese, J. Caliguiri, K. Coughlin, D. Crichton, R. Datta *et al.* (Atacama Cosmology Telescope Collaboration), Phys. Rev. Lett. **114**, 151302 (2015).
[44] A. van Engelen, B. D. Sherwin, N. Sehgal, G. E. Addison, R. Allison, N. Battaglia, F. de Bernardis, J. R. Bond, E. Calabrese, K. Coughlin, D. Crichton *et al.*, Astrophys. J. **808**, 7 (2015).
[45] A. van Engelen, R. Keisler, O. Zahn, K. A. Aird, B. A. Benson, L. E. Bleem, J. E. Carlstrom, C. L. Chang, H. M. Cho, T. M. Crawford *et al.*, Astrophys. J. **756**, 142 (2012).
[46] E. J. Baxter, R. Keisler, S. Dodelson, K. A. Aird, S. W. Allen, M. L. N. Ashby, M. Bautz, M. Bayliss, B. A. Benson, L. E. Bleem *et al.*, Astrophys. J. **806**, 247 (2015).
[47] K. T. Story, D. Hanson, P. A. R. Ade, K. A. Aird, J. E. Austermann, J. A. Beall, A. N. Bender, B. A. Benson, L. E. Bleem, J. E. Carlstrom *et al.*, Astrophys. J. **810**, 50 (2015).
[48] P. A. R. Ade, Y. Akiba, A. E. Anthony, K. Arnold, M. Atlas, D. Barron, D. Boettger, J. Borrill, S. Chapman, Y. Chinone *et al.* (Polarbear Collaboration), Phys. Rev. Lett. **113**, 021301 (2014).

[49] P. A. R. Ade, N. Aghanim, C. Armitage-Caplan, M. Arnaud, M. Ashdown, F. Atrio-Barandela, J. Aumont, C. Baccigalupi, A. J. Banday *et al.* (Planck Collaboration), Astron. Astrophys. **571**, A17 (2014).

[50] P. A. R. Ade, N. Aghanim, M. Arnaud, M. Ashdown, J. Aumont, C. Baccigalupi, A. J. Banday, R. B. Barreiro, J. G. Bartlett *et al.* (Planck Collaboratino), Astron. Astrophys. **594**, A15 (2016).

[51] P. A. R. Ade, Z. Ahmed, R. W. Aikin, K. D. Alexander, D. Barkats, S. J. Benton, C. A. Bischoff, J. J. Bock, R. Bowens-Rubin, J. A. Brevik *et al.* (T. Keck Array and BICEP2 Collaborations), Astrophys. J. **833**, 228 (2016).

[52] S. W. Henderson, R. Allison, J. Austermann, T. Baildon, N. Battaglia, J. A. Beall, D. Becker, F. De Bernardis, J. R. Bond, E. Calabrese *et al.*, J. Low Temp. Phys. **184**, 772 (2016).

[53] B. A. Benson, P. A. R. Ade, Z. Ahmed, S. W. Allen, K. Arnold, J. E. Austermann, A. N. Bender, L. E. Bleem, J. E. Carlstrom, C. L. Chang *et al.*, Proc. SPIE Int. Soc. Opt. Eng. **9153**, 91531P (2014).

[54] K. N. Abazajian, K. Arnold, J. Austermann, B. A. Benson, C. Bischoff, J. Bock, J. R. Bond, J. Borrill, E. Calabrese, J. E. Carlstrom *et al.*, Astropart. Phys. **63**, 66 (2015).

[55] K. N. Abazajian, K. Arnold, J. Austermann, B. A. Benson, C. Bischoff, J. Bock, J. R. Bond, J. Borrill, I. Buder, D. L. Burke *et al.*, Astropart. Phys. **63**, 55 (2015).

[56] See https://simonsobservatory.org/index.html.

[57] J. Liu, A. Ortiz-Vazquez, and J. C. Hill, Phys. Rev. D **93**, 103508 (2016).

[58] E. J. Baxter, J. Clampitt, T. Giannantonio, S. Dodelson, B. Jain, D. Huterer, L. E. Bleem, T. M. Crawford, G. Efstathiou, P. Fosalba *et al.*, Mon. Not. R. Astron. Soc. **461**, 4099 (2016).

[59] N. Hand, A. Leauthaud, S. Das, B. D. Sherwin, G. E. Addison, J. R. Bond, E. Calabrese, A. Charbonnier, M. J. Devlin, J. Dunkley *et al.*, Phys. Rev. D **91**, 062001 (2015).

[60] J. Liu and J. C. Hill, Phys. Rev. D **92**, 063517 (2015).

[61] D. Kirk, Y. Omori, A. Benoit-Lévy, R. Cawthon, C. Chang, P. Larsen, A. Amara, D. Bacon, T. M. Crawford, S. Dodelson *et al.*, Mon. Not. R. Astron. Soc. **459**, 21 (2016).

[62] J. Harnois-Déraps, T. Tröster, A. Hojjati, L. van Waerbeke, M. Asgari, A. Choi, T. Erben, C. Heymans, H. Hildebrandt, T. D. Kitching *et al.*, Mon. Not. R. Astron. Soc. **460**, 434 (2016).

[63] T. D. Kitching, A. F. Heavens, and S. Das, Mon. Not. R. Astron. Soc. **449**, 2205 (2015).

[64] H. Miyatake, M. S. Madhavacheril, N. Sehgal, A. Slosar, D. N. Spergel, B. Sherwin, and A. van Engelen, Phys. Rev. Lett. **118**, 161301 (2017).

[65] S. Singh, R. Mandelbaum, and J. R. Brownstein, Mon. Not. R. Astron. Soc. **464**, 2120 (2017).

[66] T. Eifler, E. Krause, P. Schneider, and K. Honscheid, Mon. Not. R. Astron. Soc. **440**, 1379 (2014).

[67] C. M. Hirata and U. Seljak, Phys. Rev. D **67**, 043001 (2003).

[68] C. M. Hirata and U. Seljak, Phys. Rev. D **68**, 083002 (2003).

[69] E. Krause and T. Eifler, arXiv:1601.05779.

[70] E. Rozo, E. S. Rykoff, A. Abate, C. Bonnett, M. Crocce, C. Davis, B. Hoyle, B. Leistedt, H. V. Peiris, R. H. Wechsler *et al.*, Mon. Not. R. Astron. Soc. **461**, 1431 (2016).

[71] C. Chang, M. Jarvis, B. Jain, S. M. Kahn, D. Kirkby, A. Connolly, S. Krughoff, E.-H. Peng, and J. R. Peterson, Mon. Not. R. Astron. Soc. **434**, 2121 (2013).

[72] G. Bernstein and D. Huterer, Mon. Not. R. Astron. Soc. **401**, 1399 (2010).

[73] Z. Ma, W. Hu, and D. Huterer, Astrophys. J. **636**, 21 (2006).

[74] P. A. R. Ade, N. Aghanim, M. Arnaud, M. Ashdown, J. Aumont, C. Baccigalupi, A. J. Banday, R. B. Barreiro, J. G. Bartlett *et al.* (Planck Collaboration), Astron. Astrophys. **594**, A13 (2016).

[75] C. Heymans, L. Van Waerbeke, D. Bacon, J. Berge, G. Bernstein, E. Bertin, S. Bridle, M. L. Brown, D. Clowe, H. Dahle *et al.*, Mon. Not. R. Astron. Soc. **368**, 1323 (2006).

[76] A. N. Taylor and T. D. Kitching, arXiv:1605.09130.

[77] C. M. Hirata, N. Padmanabhan, U. Seljak, D. Schlegel, and J. Brinkmann, Phys. Rev. D **70**, 103501 (2004).

[78] S. Bridle and L. King, New J. Phys. **9**, 444 (2007).

[79] S. Singh, R. Mandelbaum, and S. More, Mon. Not. R. Astron. Soc. **450**, 2195 (2015).

[80] P. Catelan, M. Kamionkowski, and R. D. Blandford, Mon. Not. R. Astron. Soc. **320**, L7 (2001).

[81] C. M. Hirata, R. Mandelbaum, M. Ishak, U. Seljak, R. Nichol, K. A. Pimbblet, N. P. Ross, and D. Wake, Mon. Not. R. Astron. Soc. **381**, 1197 (2007).

[82] R. Mandelbaum, C. Blake, S. Bridle, F. B. Abdalla, S. Brough, M. Colless, W. Couch, S. Croom, T. Davis, M. J. Drinkwater *et al.*, Mon. Not. R. Astron. Soc. **410**, 844 (2011).

[83] B. Joachimi, R. Mandelbaum, F. B. Abdalla, and S. L. Bridle, Astron. Astrophys. **527**, A26 (2011).

[84] J. Loveday, P. Norberg, I. K. Baldry, S. P. Driver, A. M. Hopkins, J. A. Peacock, S. P. Bamford, J. Liske, J. Bland-Hawthorn, S. Brough *et al.*, Mon. Not. R. Astron. Soc. **420**, 1239 (2012).

[85] E. Krause, T. Eifler, and J. Blazek, Mon. Not. R. Astron. Soc. **456**, 207 (2016).

[86] B. Joachimi and S. L. Bridle, Astron. Astrophys. **523**, A1 (2010).

[87] M. A. Troxel and M. Ishak, Phys. Rev. D **89**, 063528 (2014).

[88] A. Hall and A. Taylor, Mon. Not. R. Astron. Soc. **443**, L119 (2014).

[89] Y. Li, W. Hu, and M. Takada, Phys. Rev. D **89**, 083519 (2014).

[90] C.-T. Chiang, C. Wagner, F. Schmidt, and E. Komatsu, J. Cosmol. Astropart. Phys. 05 (2014) 048.

[91] Y. Li, W. Hu, and M. Takada, Phys. Rev. D **90**, 103530 (2014).

[92] M. Takada and D. N. Spergel, Mon. Not. R. Astron. Soc. **441**, 2456 (2014).

[93] E. Schaan, M. Takada, and D. N. Spergel, Phys. Rev. D **90**, 123523 (2014).

[94] A. van Engelen, S. Bhattacharya, N. Sehgal, G. P. Holder, O. Zahn, and D. Nagai, Astrophys. J. **786**, 13 (2014).

[95] S. J. Osborne, D. Hanson, and O. Doré, J. Cosmol. Astropart. Phys. 03 (2014) 024.
[96] T. Eifler, P. Schneider, and J. Hartlap, Astron. Astrophys. **502**, 721 (2009).
[97] E. Sellentin and A. F. Heavens, Mon. Not. R. Astron. Soc. **456**, L132 (2016).
[98] M. White and N. Padmanabhan, J. Cosmol. Astropart. Phys. 12 (2015) 058.
[99] J. Carron, Astron. Astrophys. **551**, A88 (2013).
[100] D. Foreman-Mackey, D. W. Hogg, D. Lang, and J. Goodman, Publ. Astron. Soc. Pac. **125**, 306 (2013).
[101] D. Huterer, M. Takada, G. Bernstein, and B. Jain, Mon. Not. R. Astron. Soc. **366**, 101 (2006).
[102] A. Hall and A. Taylor, Mon. Not. R. Astron. Soc. **443**, L119 (2014).
[103] N. E. Chisari, J. Dunkley, L. Miller, and R. Allison, Mon. Not. R. Astron. Soc. **453**, 682 (2015).
[104] M. A. Troxel and M. Ishak, Phys. Rev. D **89**, 063528 (2014).
[105] P. Larsen and A. Challinor, Mon. Not. R. Astron. Soc. **461**, 4343 (2016).
[106] L. Amendola, S. Appleby, D. Bacon, T. Baker, M. Baldi, N. Bartolo, A. Blanchard, C. Bonvin, S. Borgani, E. Branchini *et al.*, Living Rev. Relativ. **16**, 6 (2013).
[107] L. Wolz, M. Kilbinger, J. Weller, and T. Giannantonio, J. Cosmol. Astropart. Phys. 09 (2012) 009.